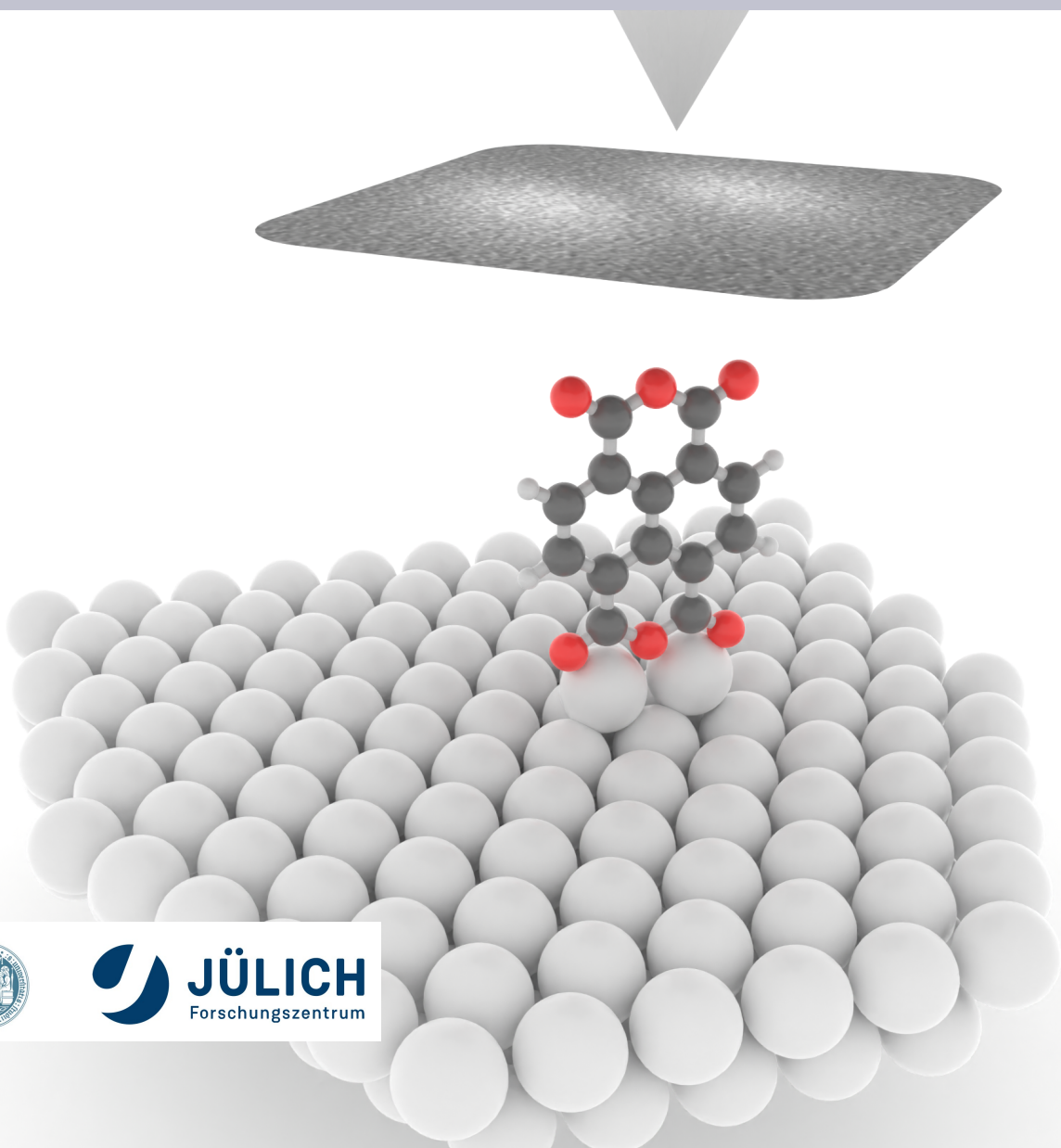


Kondo Effect in a Standing Molecule

Scanning Tunneling Spectroscopy Study of the Kondo Effect in a Standing NTCDA Molecule at Millikelvin Temperature

MSc thesis

Valentin Maissen



Kondo Effect in a Standing Molecule

Scanning Tunneling Spectroscopy
Study of the Kondo Effect in a
Standing NTCDA Molecule at
Millikelvin Temperature

A thesis submitted in partial fulfillment
of the requirements for the degree of

Master of Science
in
Physics

Author:

Valentin Maissen

Student ID:

7336712

First corrector:

Prof. Ruslan Temirov

Second corrector:

Prof. Thomas Michely

Project duration:

Nov. 2022 – Dec. 2023



Contents

1	Introduction	1
2	Background	3
2.1	Scanning Tunneling Microscopy	3
2.1.1	Tunneling	3
2.1.2	Measurement Techniques	6
2.2	The Kondo effect	10
2.3	NTCDA, PTCDA and the Kondo effect	12
3	Methods	15
3.1	The millikelvin STM at FZ Jülich	15
3.2	Sample Preparation	17
3.3	Molecular Manipulation	18
3.4	Data Analysis	23
3.4.1	Spectrum Processing	23
3.4.2	Spectrum Fitting	23
4	Results	25
4.1	Spin g-factor	25
4.2	Magnetic Splitting of the Kondo Peak	26
4.3	Line Width Evolution of the Kondo Peak	29
4.4	Temperature evolution of Kondo peak sharpness	33
4.5	High Magnetic Field: Visualizing the Crossover	34
4.6	Differences in the Kondo Temperature	36
4.7	Junction Temperature	37
4.8	Conclusion and Comparison to PTCDA	40
4.9	Outlook	42

1. Introduction

The spin is one of the fundamental properties of matter. In the 1920s, Stern and Gerlach for the first time observed the quantization of angular momentum [1] and some years later Pauli introduced the theoretical formalism to describe the electron spin in wave mechanics [2] that was later extended to relativistic quantum mechanics by Dirac [3]. In the decades that followed, magnetic resonance was pioneered by Rabi, the Lamb-shift lead to the renormalization of quantum electrodynamics and experimental progress pushed the accuracy of determining the electron spin g-factor to the thirteenth decimal place [4].

The orders in magnitudes of precision obtained by particle physics experiments cannot be reached in condensed matter physics, where uncountable degrees of freedom are involved - 1 cm³ of a metal contains about 10²³ atoms. On the other hand, the large number of degrees of freedom allows for the emergence of collective phenomena like superconductivity, Bose condensates, lattice vibrations or the Kondo effect. The latter describes the interaction of a localized spin with the conduction electrons of a metal that, characterized as a whole, form a many-body-state.

The invention of the scanning tunneling microscope in the 1980s [5] opened the door to study surfaces on the nanoscale - atom for atom. This allowed for the imaging of the Si(111) 7x7 reconstructed surface [6], the visualization of electron wave functions in a confining potential [7], the imaging of chemical bonds [8, 9], creation of nanoscale storing units [10], measurement of single atom electron spin resonance [11] and quantum-coherent manipulation [12].

Apart from the atomic resolution that can be achieved, the scanning tunneling microscope is unique for its ability to manipulate surfaces on the nanoscale. This had a great impact on Quantum Nanoscience, a field of research that aims at creating devices that exploit quantum mechanical effects. The building blocks, atoms and molecules residing on the surface, could now be moved to different atomic environments and be combined to form new structures. This enables detailed measurements of a single structure in various configuration.

A well studied example for this endeavor are the organic molecules PTCDA and NTCDA, that were investigated in isolation on the surface [13], in the monolayer configuration [14, 15], clamped between the measuring tip and the surface [16, 17], hanging on the tip apex [18] and standing upright on the surface [19, 20].

The latter configuration is of particular interest, since the molecule is somewhat isolated from the surface conduction electrons, and hosts a single free spin. This makes it an well described model system, considering that we are dealing with more than a dozen atoms on a metal surface.

The Kondo effect in the standing PTCDA molecule has been studied [19], but not yet in NTCDA. As the crossover temperature of the Kondo effect is a proxy for the hybridisation strength of the molecule with the surface, its determination can be of use for future coherent application [21, 22].

The aim of this thesis is to investigate the Kondo effect in the standing NTCDA molecule on an Ag(111) surface and compare it to PTCDA. These molecules have a very similar chemical structure - they basically only differ in size. Potential physical differences can thus be attributed to a limited parameter space. This might prove useful, as the theoretical modeling of these molecules is not yet fully mature, especially when it comes to the notoriously complicated Kondo effect [23].

Going beyond that, my personal motivation for this work is also based on the desire to understand the world of scientists. After numerous years in lecture halls, it was exciting to get serious, to be part of scientific discussions, to go to conferences, to experience scientific passion and dissapointment in oneself and in others and to be responsible for the operation of a Million-Dollar-Machine that can actually make atoms visible. I aim at putting on paper what I learned last year, yet knowing that the major insights are not to be written down.

In the first chapter the theoretical basis of the scanning tunneling miscroscope - the experimental device used - is introduced and a general background of the physical concepts is provided. After covering the experimental methods and data analysis in the second chapter, we the results of various measurements are presented in the third chapter.

2. Background

2.1 Scanning Tunneling Microscopy

The working principle of a scanning tunneling microscope (STM) is remarkably simple: Applying a voltage bias between a sharp metal tip and a conducting surface results in a tunneling current, if the distance between the objects is sufficiently small. The basic setup is sketched in figure 2.1. The tip can move in xyz-direction because it is attached to a piezoelectric scanner, which can be operated by applying high voltage. The tunneling current is strongly sensitive to the tip-sample distance and will therefore change as the tip moves around laterally (scans) according to the structure of the surface. By mapping the conductivity during the scan of an area, a ‘microscopic’ image of a surface can be obtained. Some general concepts of the STM will be described in the following.

2.1.1 Tunneling

Electron tunneling describes the process of an electron overcoming a potential barrier even though its energy is not large enough from the classical point of view. The transmission probability generally is inversely exponentially dependent on the width d of the potential barrier, $T \propto \exp(-2d)$ [25]. This dependence on d was what made Binnig and Rohrer, the inventors of the STM [5], assume that it could be a sensitive way of measuring the tip-sample distance.

As the exact ‘wave-matching’ approach is in general very difficult, approximate methods are preferred for real systems like the tip-sample junction. Bardeen [26] developed a time-dependent tunneling theory to calculate the current I . Assuming a negatively biased tip, I is calculated via the overlap of the possible initial tip wave functions $\sum_i \psi_{i,t}$ with energy E_i and the possible final sample wave functions $\sum_f \psi_{f,s}$ with energy E_f using Fermi’s ‘golden rule’:

$$I = \frac{4\pi e}{\hbar} \sum_{i,f} |M_{fi}|^2 \delta(E_f - E_i),$$

where \hbar is the reduced Planck constant, e is the elementary charge, $\delta(x)$ the Dirac delta function and $|M_{fi}|$ the tunneling matrix element given by [26]

$$M_{fi} = \frac{-\hbar^2}{2m_e} \int d\mathbf{S} \cdot (\psi_{i,t}^* \nabla \psi_{f,s} - \psi_{f,s}^* \nabla \psi_{i,t}),$$

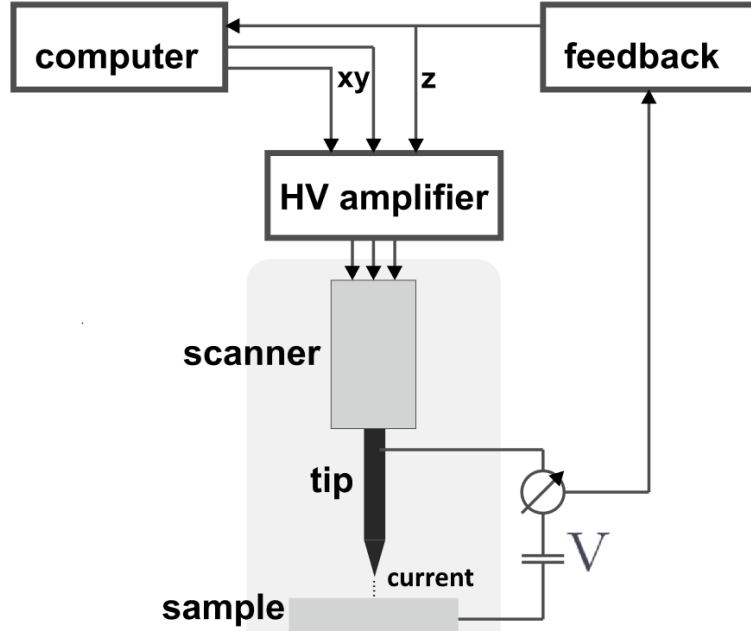


Figure 2.1: Working principle of the STM: Electrons tunnel between a sharp metal tip and a conducting sample. By applying high voltage to the piezoelectric scanner, the tip can move in xyz-direction. During lateral movement a feedback loop can keep the current constant by adjusting the voltage in z-direction (see section 2.1.2) (figure taken from [24]).

with m_e being the electron mass. The surface integral is evaluated over an arbitrary surface lying within the vacuum between the two electrodes. The delta function with the energies of the initial state E_i and the final state E_f describes the conservation of energy for the elastic case. To solve the integral one needs all possible wave functions of the sample and tip (within the energy range corresponding to the applied bias). As the exact electronic shape of the tip is usually unknown, further approximation is needed. Tersoff and Hamann [27] modeled the tip simplistically as a sphere and neglected wave functions with angular dependence (*s-wave approximation*). In the limit of a low applied bias and at low temperature, they obtained

$$I \propto V \cdot n_t(E_F) \cdot \sum_s |\psi_s(\mathbf{r}_0)|^2 \delta(E_s - E_F), \quad (2.1)$$

V being the applied bias voltage, $n_t(E_F)$ the density of states of the tip at the Fermi energy and $\psi_s(\mathbf{r}_0)$ the wave function of the sample at the tip position \mathbf{r}_0 . The term behind the sum can be interpreted as the local density of states ($LDOS(E_F)$) of the sample, i.e. the density of states at E_F evaluated at the center of the spherical tip orbital $n_s(E_F, \mathbf{r}_0)$. As wave functions decay exponentially into vacuum, $\psi_s(z) \propto \exp(-\kappa z)$ (κ is the decay constant $\kappa = \sqrt{2m\Phi/\hbar}$, corresponding to an effective barrier height Φ) [25], one also obtains the exponential dependence of the tunneling current on the tip-sample distance: $I \propto |\psi_s(\mathbf{r}_0)|^2 \propto \exp(-2\kappa d)$.

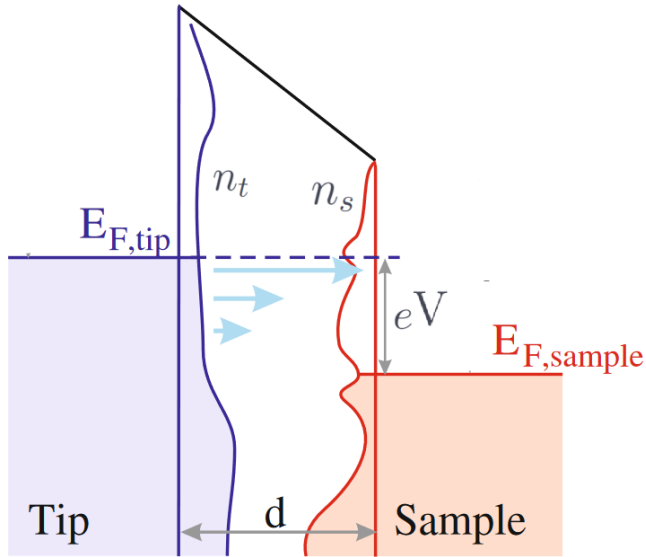


Figure 2.2: Energy levels in STM: The tunneling current is exponentially dependent on the tip-sample distance d and the applied bias voltage V , as illustrated by the blue horizontal arrows. The density of states of the tip n_t and the sample n_s are colored if occupied and blank if unoccupied. If the bias polarity were inverted, the energy levels would switch and the current would flow from sample to tip (taken from [28]).

Applying this to typical STM values ($d = 5 \text{ \AA}$, $\Phi = 4 \text{ eV}$) [28] justifies the rule of thumb, that a distance shift of $\Delta d = 1 \text{ \AA}$ changes the current by one order of magnitude.

If higher bias voltages are taken into account, additional tip and surface wave functions have to be considered. Neglecting the distortion of the wave functions and the modification of the energy eigenvalues [29], a finite bias V only enters by shifting the LDOS of the surface relative to the tip by eV . Again assuming a biased tip, 2.2 can be generalized to the following expression:

$$I \propto \int_0^{eU} n_t(\epsilon - eU) \cdot n_s(\epsilon) \cdot T(E, V) d\epsilon, \quad (2.2)$$

where $T = \exp(-2\sqrt{2m_e(eV/2 - E)}/\hbar \cdot d)$ and all energies are measured with respect to the Fermi level. Note that this equation also makes use of the zero-temperature approximation, because the Fermi-distribution of the density of states is taken to be a step function.

The tunneling current in the more general case is therefore proportional to the convolution of the LDOS of the tip and the density of states of the sample. The exponential term $T(E, V)$ illustrates that the tunneling current is exponentially dependent not only on the tip-sample distance d but also on the applied bias voltage \sqrt{V} . The tunneling behavior is sketched in figure 2.2. The tunneling current is therefore dependent both on the tip-sample distance d as well as on

the sample density of states, which can render its analysis difficult: An adatom on a metal surface can look like a depression, if the integral of the density of states in the bias window (equation (2.2)) is smaller than the according value for the metal surface.

2.1.2 Measurement Techniques

The STM is a versatile tool that provides different measurement schemes. Apart from imaging techniques, also spectroscopic measurements can be performed. The following section will give a brief overview of the most important techniques.

Constant Height Imaging

As the LDOS on a conducting surface is not constant laterally, the current during a scan will be neither. By moving the tip across the sample surface at constant height, the resulting evolution of the current directly reflects the energy integrated sample LDOS at this particular height. This straightforward interpretation comes with technical difficulties: it can only be applied on extremely flat (and therefore well known) surfaces to avoid tip crashes, the thermal drift of the piezo scanner needs to be taken into account as well as the tilt between sample and tip. In order to directly obtain the LDOS, the dI/dV signal (details see below) can be measured during the constant height scan. This significantly reduces the scanning speed, as several periods of the oscillating bias voltage need to be measured at each pixel.

Constant Current Imaging

Another approach is to keep the current constant during a scan by adjusting the z-position (height) of the tip. This is done by continuously adjusting the voltage V_z to the z piezoelectric drive with a feedback loop, that aims at keeping $I = \text{const.}$ (see figure 2.1). In this case, the scanning speed is limited by the finite response time of the feedback loop. Mapping V_z will accordingly yield the 'topography', that is, the contour of constant density of states of the sample. As the current is kept constant, tip crashes are avoided and rough, unknown surfaces can be scanned safely.

The response time of the feedback loop can be tuned to a slower reaction, which can be useful to scan large areas quickly and safely. Then the feedback loop does not react to single atoms but to long range height changes like a tilt in the surface. A slower response time also can be used to avoid driving the eigenfrequency of a vibrating tip-sample system, which could lead to tip crashes. This has to be considered for experiments over the standing NTCDA molecule.

Scanning Tunneling Spectroscopy

The STM can also be used as a spectroscopic tool, because of the bias-dependence in the tunneling current mentioned above: At zero bias the Fermi level of the tip and the sample are aligned. If now a bias is applied with negative polarity

to the tip, the net current arises from electrons that tunnel from the occupied states of the tip into unoccupied states of the sample (again see figure 2.2). For inverse polarity, the process is accordingly inverted. Therefore, the bias polarity determines whether unoccupied or occupied sample electronic states are probed. In scanning tunneling spectroscopy (STS), the aim is to measure the density of states of the sample. This is accomplished by measuring the current-to-voltage characteristic of the tunneling junction: If dV is added to the bias, all tip states are shifted up and an additional dI contributes to the current (new long blue line appears at $E_{F,tip}$ in figure 2.2). The additional current per voltage increase is approximately given by the integrand in equation (2.2) taken at the upper limit of the integral $\epsilon = eV$:

$$\frac{dI}{dV} \propto n_t(0) \cdot n_s(eV) \cdot T(E, V) \propto n_s(eV) \quad (2.3)$$

The second relation holds for the approximation of n_s and T being voltage independent. The resulting dI/dV curve is therefore proportional to the LDOS of the sample.

Instrumentally, dI/dV can be accessed by superimposing the bias voltage V with a modulation frequency $V_m \cos(\omega t)$. Having the feedback loop disabled, the measured modulated current will in general be

$$I(t) = f(V + V_m \cos(\omega t)),$$

where $f(\cdot)$ describes the $I - V$ relation of the junction. A lock-in amplifier measuring the amplitude of the modulated current can then read out the dI/dV signal. To illustrate the general working principle, a hypothetical $I - V$ curve is sketched in figure 2.3: The sinusoidal modulation at bias voltage V_1 induces a lower amplitude of the modulated current, compared to the modulation at V_2 , where the slope of the $I - V$ curve is larger.

More rigorously, the Taylor expansion of $f(V + V_m \cos(\omega t))$ around V yields [28]

$$\begin{aligned} I &= \sum_{k=0}^{\infty} \frac{V_M^k}{k!} \frac{d^k f(V)}{dV^k} \cos^k \omega t \\ &= f(V) + V_M \frac{df(V)}{dV} \cos \omega t + \frac{V_M^2}{2} \frac{d^2 f(V)}{dV^2} \cos^2 \omega t \\ &\quad + \frac{V_M^3}{6} \frac{d^3 f(V)}{dV^3} \cos^3 \omega t + \frac{V_M^4}{24} \frac{d^4 f(V)}{dV^4} \cos^4 \omega t + \dots \end{aligned} \quad (2.4)$$

The $\cos^n(\omega t)$ terms can be expressed as a sum of cosines with an up to n -times higher frequency, using the trigonometric identity

$$\cos^n(\omega t) = \frac{1}{2^n} \sum_{k=0}^n \binom{n}{k} \cos((n-2k)\omega t).$$

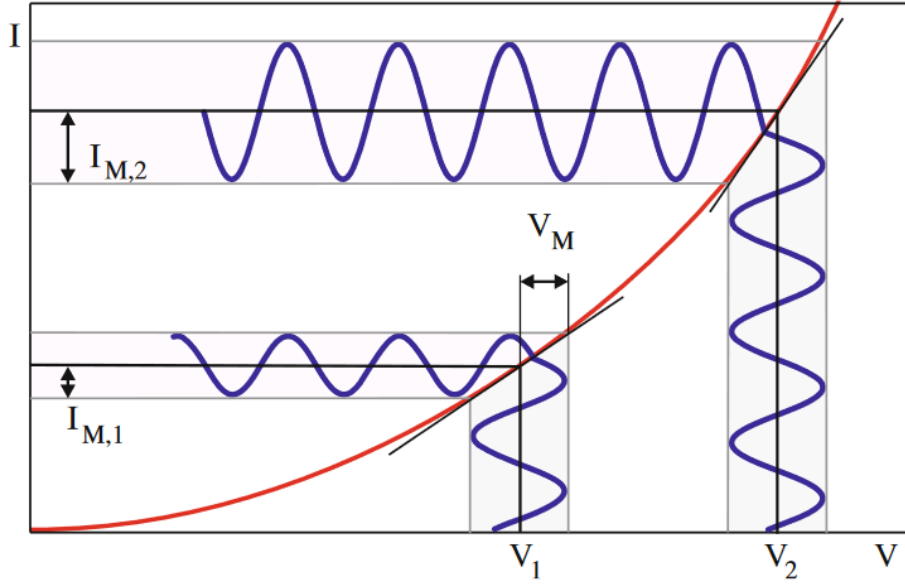


Figure 2.3: The voltages V_1 and V_2 are modulated with the same modulation amplitude V_M . The resulting modulated currents $I_{M,2}$ and $I_{M,1}$ differ, as the slope of the $I - V$ curve is different at V_1 and V_2 (taken from [28]).

Rearranging the cosine terms according to the frequencies, one obtains

$$\begin{aligned}
 I = \sum_{k=0}^{\infty} \frac{V_M^k}{k!} \frac{d^k f(V)}{dV^k} \cos^k \omega t = \\
 1 \left[f(V) + \frac{d^2 f(V)}{dV^2} \frac{V_M^2}{4} + \dots \right] + \\
 + V_M \cos \omega t \left[\frac{df(V)}{dV} + \frac{d^3 f(V)}{dV^3} \frac{V_M^3}{8} + \dots \right] + \\
 + \frac{1}{4} V_M^3 \cos 2\omega t \left[\frac{d^2 f(V)}{dV^2} + \frac{d^4 f(V)}{dV^4} \frac{V_M^4}{12} + \dots \right] + \dots
 \end{aligned} \tag{2.5}$$

Neglecting the higher order terms in the square brackets then directly shows that the amplitude of the signal at n -times the modulation frequency is proportional to the n th derivative of the I-V-curve at V . Therefore, the lock-in amplifier set to the bias modulation frequency directly measures the first derivative of the $I - V$ curve. In the same manner also higher harmonics can be used to measure higher derivatives of the $I - V$ curve, which can be useful for example to detect the precise bias value of spectral features.

An example for a dI/dV spectrum that reflects the density of states of the sample is shown in figure 2.4: Ag(111) has a surface state with a band edge below the Fermi energy at -63 mV [30]. The surface state exists due to the broken periodicity of the crystal at the surface [31]. The electrons in the surface state form a nearly free two-dimensional electron gas which implies a constant density of states [32]. This can be directly seen in the constant dI/dV spectrum above

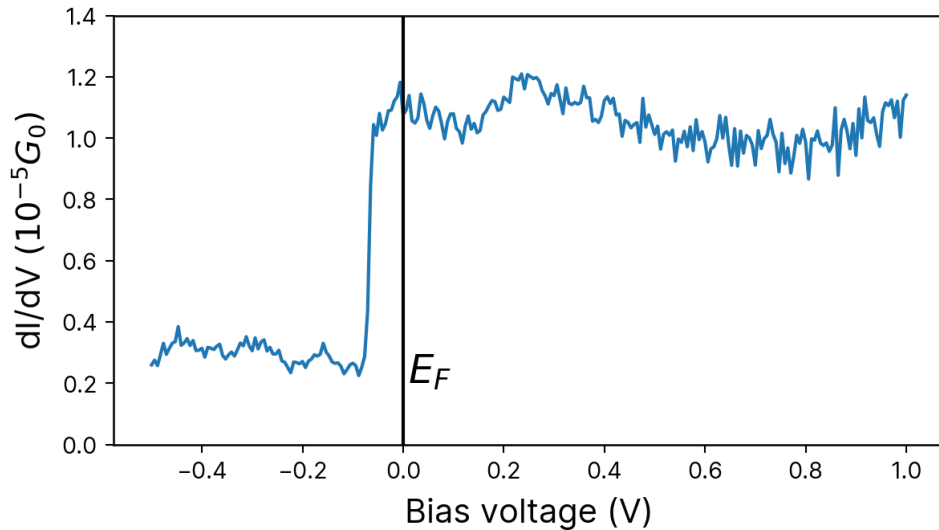


Figure 2.4: Ag(111) surface state: The dI/dV spectrum shows a step at -63 mV that is attributed to the onset of the surface state, therefore directly reflecting the density of states of the sample. Spectrum aquired at $T = 1\text{ K}$, $V_{mod} = 5\text{ mV}$, $f_{lock-in} = 187\text{ Hz}$.

the band edge. The significant step in the dI/dV curve has been used in this work to determine the quality of the tip: For the approximation in equation (2.2) to hold, a flat density of states of the tip around the Fermi energy is desirable. This can be tested best by STS measurements at negative bias, as the new tip states entering the bias window are probed with a large transmission factor (invert energy levels in figure 2.2). Therefore, the flatness of the dI/dV curve around the step is a measure for the quality of the tip for STS experiments.

Inelastic Tunneling Spectroscopy

While STS gives insight to the LDOS of the sample, also other electronic mechanisms can be studied by spectroscopy. Itself rather being a method than a technique, inelastic tunneling spectroscopy (IETS) can be used to study the vibrational modes or the spin excitation of a nanostructure [33, 34]. The principle of IETS is displayed in figure 2.5a: The tip is positioned over the structure of interest, z-feedback is disabled and the bias voltage between tip and sample is ramped. Above an excitation energy $e|V| > \hbar\omega$ the tunneling electron can excite a degree of freedom (vibration, spin flip ...) of the object in the junction via an inelastic tunneling process. When the inelastic tunneling path opens above the threshold voltage, the tunneling current increases, because now both the elastic and the inelastic path contribute to the current. The elastic tunneling current is smeared by the Fermi distribution of the tip due to the finite temperature, which will be discussed below. On the other hand, the inelastic tunneling current in vicinity of the threshold voltage is additionally smeared by the Fermi distribution of the sample, where it tunnels into, see figure 2.5a. Therefore, the step in the dI/dV curve that marks the onset of the inelastic tunneling as shown in figure 2.5b is more broadened than the other features in the dI/dV spectra [35].

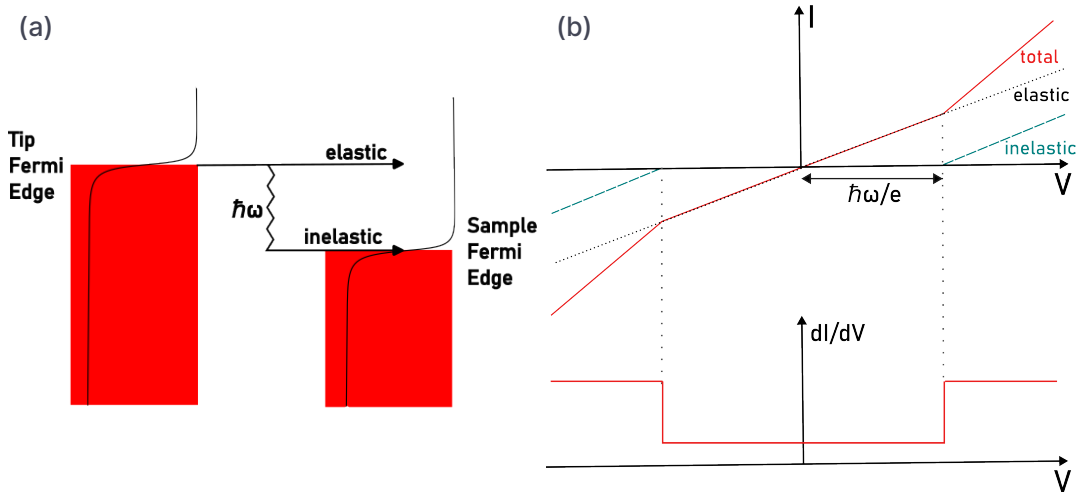


Figure 2.5: Principle of inelastic tunneling spectroscopy: **(a)** If the shift between the Fermi edges of tip and sample exceeds the excitation energy $\hbar\omega$, electrons can tunnel inelastically by exciting a degree of freedom in the junction. The elastic tunneling current is smeared by the tip temperature broadening, whereas the inelastic tunneling current is also smeared by the sample temperature broadening. **(b)** The resulting dI/dV curve shows a step at the excitation energy $e|V| = \hbar\omega$.

Remarkably, the physics that can be examined using STS is not limited to simple electron density of states and the degrees of freedom of nanostructures. In the late 1990s, another type of phenomenon was identified using STS, when Madhavan et al. [36] explained a feature in the dI/dV curve around zero bias: The Kondo effect, a localized many-body-state around the Fermi edge. As this phenomenon is the main topic in this thesis, it will be covered in more detail in the following.

2.2 The Kondo effect

Usually, decreasing temperatures enhance the electrical conductivity in metals, which is caused by the increased freezing out of phonons [32]. But already in 1934 a resistance minimum was observed in gold as a function of temperature, implying the existence of new type of scattering mechanism [37]. The phenomenon also appeared in other metals but remained a puzzle for another 30 years until the effect was recognized to be associated with magnetic impurities in the metallic host [38]. Shortly thereafter it was Jun Kondo who showed how spin-exchange scattering at these impurities can result in a resistivity contribution of $\log(T)$. This behavior was termed *Kondo effect*.

Among other approaches the Kondo effect can be described by the Anderson single impurity model [40], in which an impurity is embedded in a nonmagnetic

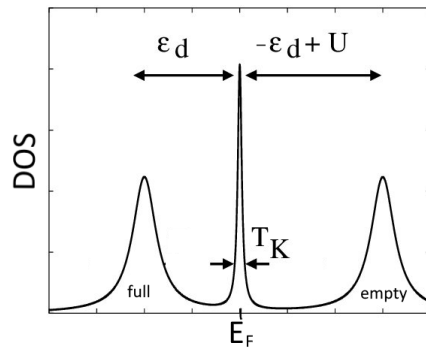


Figure 2.6: Impurity DOS in the single-impurity Anderson model: A half-filled orbital with Coulomb repulsion U , where the occupied state has a binding energy of ϵ_d . The Kondo resonance is generated by spin-flip scattering processes between the impurity and the host spin bath. The width of the resonance can be used as a definition for the Kondo Temperature T_K (taken from [39]).

metallic host. The full electronic structure of the impurity is simplified by assuming only a single orbital state that can be filled with zero, one or two electrons. The singly occupied state is located below the Fermi energy at binding energy ϵ_d and is separated by the Coulomb repulsion energy U from the state occupied with two electrons with opposite spins, as shown in figure 2.6. In this setting, exchange processes occur with the host spin bath. These processes involve either emptying and refilling the lower lying state or adding a second electron and subsequently removing one. The final state may have an opposite spin compared to the initial one.

Quantum mechanics allows these transitions as virtual processes within a short time frame dictated by the Heisenberg uncertainty principle. Within this timescale, the energy conservation is violated and the electron can tunnel from the occupied state to the Fermi level of the host, or vice versa, without energy input. The resulting spin exchange between the impurity and the host spin bath modifies the energy spectrum of the system. Taking many such processes together, a new ground state with lower total energy, the so-called Kondo resonance, is generated very close to the Fermi energy (see figure 2.6). As this state also scatters conduction electrons, an increase in resistivity can be observed. This effect increases with decreasing temperature, as the Fermi distribution narrows and more conduction electrons will scatter. At 0 K the many-body state is a nonmagnetic Kondo singlet state in which the spin of the impurity is completely screened.

The thermal transition into this state is a continuous crossover and not a discrete phase transition. The crossover temperature is called *Kondo temperature* T_K . Due to the continuous nature of the transition, various definitions of T_K exist that differ by a factor of order one. In this work Γ_0 , the half width of the Kondo peak at 0 K, is used as a definition for T_K , i.e. $k_B T_K = \Gamma_0$. For the sake of completeness, we mention another definition, namely Wilson's thermodynamic

Kondo temperature $T_{K,W}$. It is defined implicitly by $k_B T_K \cdot \chi_{imp}(T_K) = 0.7(g\mu_B)^2$, where $\chi_{imp}(T_K)$ is the impurity susceptibility [41, chapter 5]. It is commonly used also in STM literature [42–44] and related to Γ_0 by $T_{K,W} = 3.92T_K$ [43].

Different theoretical approaches have been developed to describe the Kondo effect, among them exact methods like the modified Bethe ansatz [45] or numerical renormalization theory [46]. The latter has been used recently to test the Anderson model by experimentally precisely controlling the model parameters [47]. In our analysis we will make use of a perturbative Anderson-Appelbaum approach [48] that models tunneling between two electrodes via a magnetic impurity. The processes in third order exchange interaction lead to a temperature-broadened logarithmic resonance in the conductance (=Kondo peak), which can be directly compared to the obtained dI/dV spectra. In the strong coupling regime ($T < T_K, B = 0$) the third and higher order scattering terms become the dominant processes and perturbation theory breaks down. Using this model, the transition from weak to strong coupling with decreasing temperature can thus be observed.

The exact footprint of the Kondo resonance in STS depends on the experiment: there are different tunneling channels for the tip electrons: directly from tip to sample, via the Kondo resonance or indirectly via a spin flip in the hybridized state of the adatom. As the first two paths have the same start and end situation (spin of the tunneling electron is conserved), the tunneling current is governed by the quantum interference of these two channels. In the model proposed by Frota and Oliveira based on the Anderson model [49] the phase Φ regulates the resonance shape:

$$\rho_{frota}(V) \propto \Im \left[e^{i\Phi} \sqrt{\frac{i\Delta_k}{eV - E_K + i\Delta_k}} \right],$$

where Δ_k is related to the halfwidth at half-maximum Γ by $\Gamma = \sqrt{3 + \sqrt{12}}\Delta_k \approx 2.524\Delta_k$ [43] and E_K is the position of the resonance.

Gruber et al. [50] showed that the Frota line shape is a better approximation for the Kondo resonance in STS in case of low temperature and narrow modulation broadening, compared to the Fano shape [51]. In the following, the Frota line shape will be used in the analysis.

The Kondo effect has been investigated by STS for metal adatoms [36, 52–54] and on a large variety of adsorbed molecules (first observation see [55]). Two well studied organic molecules in that context are NTCDA and PTCDA, which will be described in the following.

2.3 NTCDA, PTCDA and the Kondo effect

1,4,5,6-naphthalene tetracarboxylic dianhydride (NTCDA) and 3,4,9,10-perylene tetracarboxylic dianhydride (PTCDA) are planar organic molecules. Their geometry and chemical structure are sketched in figure 2.7. Upon evaporation on

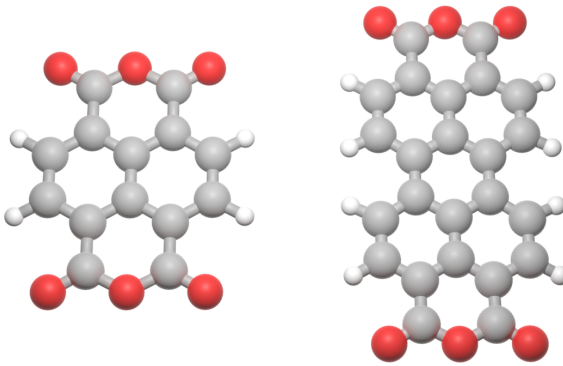


Figure 2.7: On the left is the ball-stick model of NTCDA, on the right of PTCDA. The red balls represent oxygen, the gray ones carbon and the white ones hydrogen.

Ag(111) - the sample used in our experiments - they chemisorb and can form commensurate monolayer islands. The chemisorption of PTCDA leads to a substantial charge transfer of about 2 e into the former lowest unoccupied molecular orbital (LUMO) of the free molecule. A charge transfer occurs also for NTCDA [56], but it is less well understood. Depending on the adsorption geometry NTCDA shows a Kondo effect [57, 58], implying an occupation of less than two.

The hybridization of the molecules can be minimized by gradually lifting the molecule from the surface after establishing a well-defined contact to it from the tip (see section 3.3). The lifting changes the occupancy of the LUMO and thus a situation of a singly occupied orbital is reached which is a prerequisite for the Kondo effect [16]. For PTCDA, the Kondo effect has been analyzed [23], and it was found that the Kondo temperature drops substantially when the molecule approaches the vertical configuration.

By using two silver atoms as a foundation, the molecule can reside in the vertical position also when the tip gets retracted (see section 3.3). This manipulation has been reported for both molecules [19], but a more detailed analysis was recently conducted for PTCDA by Esat et al. [20]. As this report is the basis for our analysis and will be used as a comparison, the results are described in more detail.

The standing PTCDA molecule was identified as an $S = 1/2$ -spin system by extracting the energies of the Zeeman splitting at high magnetic fields. The determination of the critical magnetic field that is needed to split the Kondo peak yielded a Kondo temperature of $T_K = 291\text{ mK}$, see figure 2.8a. Using another method to extract the Kondo temperature, namely from the width of a single fitted Kondo peak, the value $T_K = 1280\text{ mK}$ was obtained. The value mentioned in ref. [20] is four times lower, but uses a definition of T_K that is not consistent, as far as I judge it. The physical crossover from the strong to the weak coupling Kondo regime was observed by fitting a spectral function (using the perturbation model introduced in section 2.2) to the dI/dV curves measured with a 7 T magnetic field at various temperatures. The evolution of the fit parameters $J\rho$ describing the

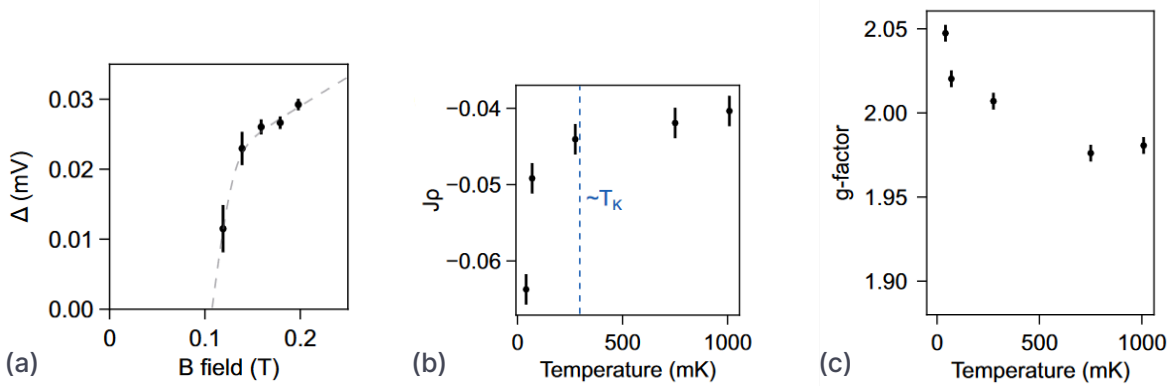


Figure 2.8: Previous results from the Kondo study on the standing PTCDA molecule. **(a)** The widths Δ of the splitted Kondo peak at different B -fields lead to the determination of the critical field $B_C = 108$ mT, that corresponds to $T_K = 74$ mK. **(b)** and **(c)**: Parameters of the Anderson-Appelbaum perturbative model as a function of temperature: **(b)** $|J\rho|$ and **(c)** the g-factor of the $S = 1/2$ -spin. The crossover from the strongly to the weakly interacting Kondo regima is visible at around 300 mK. Data aquired at 7 T. All Figures taken from [20].

coupling strength of the Kondo system to the sample, and the spin g-factor of the impurity spin is shown in figures 2.8b and 2.8c. Below 300 mK $|J\rho|$ as well as the g-factor significantly increase, indicating a progressive breakdown of the applied perturbation approach.

3. Methods

3.1 The millikelvin STM at FZ Jülich

All experiments were conducted on the Jülich Quantum Microscope 1.0. A detailed description of the microscope has been published elsewhere [59], therefore we will restrict ourselves to a general overview.

The outstanding characteristic of the STM is its cooling technique: Using adiabatic demagnetization refrigeration (ADR), a minimal temperature of 27 mK can be reached. This technology is based on the magnetocaloric effect in paramagnets that possess a large magnetic entropy at low temperature. The working principle of ADR is sketched in figure 3.1 and the concrete temperature evolution of one cooling cycle of our STM is shown in figure 3.2: By applying a strong magnetic field (6 T) to the paramagnet, the magnetic entropy is minimized. The paramagnet is subsequently cooled to 1 K using a 1K-pot, then gets thermally decoupled from the pot using heat switches (HS), such that the conditions are adiabatic. As the magnetic field is then turned off, the magnetic entropy will increase again and the temperature will decrease, as $TS = U = \text{const}$. This drop in temperature is a single-shot process with $27 \text{ mK} < T < 100 \text{ mK}$ for 24h. If the ADR magnet is not turned off at once, a constant temperature can be maintained by a software feedback loop controlling the temperature by adjusting the magnetic field.

The paramagnets of choice for our STM was a combination of gadolinium gallium garnet (GGG, $Gd_3Ga_5O_{12}$) and ferric ammonium alum (FAA, $NH_4Fe(SO_4)_4$). While FAA has a higher residual entropy and thus cools to lower temperatures, the spin packing density and therefore the holding time of GGG is larger. The STM body is directly thermalized to FAA. By fitting a spectrum of the superconducting gap, measured on Al(100) with a PtIr tip, an effective temperature of $T_{\text{eff}} = 157 \text{ mK}$ was obtained. In a detailed analysis, which considers interaction of the junction with the radiation environment ($P(E)$ -theory), the actual temperature of the tip was determined to be well described by $T_{\text{tip}} = T_{\text{ADR}} + 45 \text{ mK}$ [61], where T_{ADR} is the measured temperature of the FAA crystal. In this work, T_{tip} will be used to correct for the temperature smearing (see section 3.4.2).

The whole setup is located in a vibrationally isolated, electromagnetically shielded laboratory [62]. No mechanical pumps are needed during measurement, as the 1K-pot is operated with a high-capacity activated charcoal cryopump. The

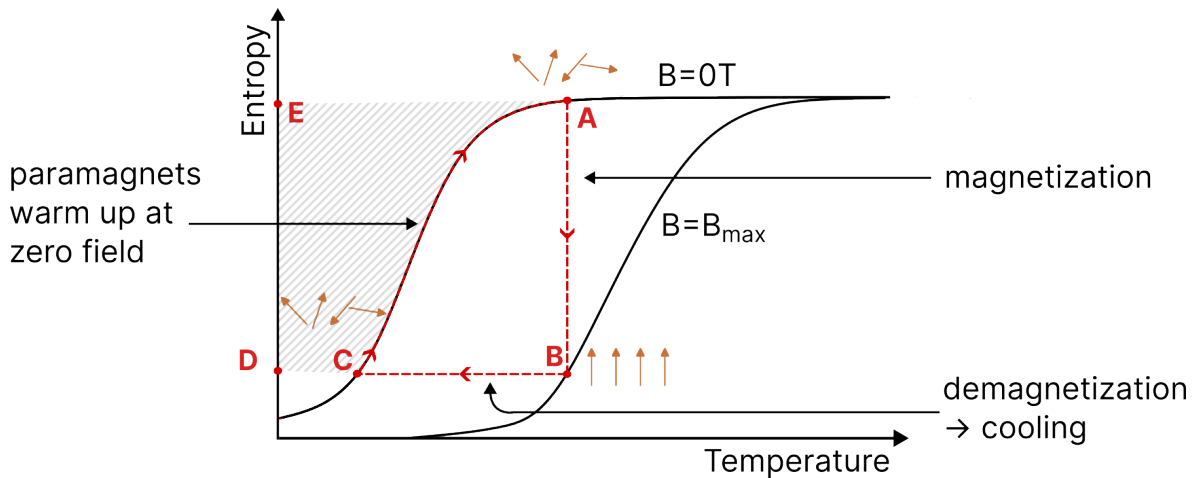


Figure 3.1: Entropy of a paramagnet versus temperature for magnetic fields. The refrigeration process starts at A. The line AB represents an isothermal magnetization. The heat produced along AB is delivered to a heat sink, the 1K-pot in our case. After thermal isolation (HS OFF in figure 3.2), the crystal is adiabatically demagnetized (line BC) and reaches the minimal temperature. Eventually it warms up along the entropy curve at the final magnetic field, which is zero in this example. The heat of magnetization is given by the area of the rectangle ABDE, the cooling power by the shaded area [60]. The orange arrows represent the configurational entropy of the spin orientations in the paramagnets.

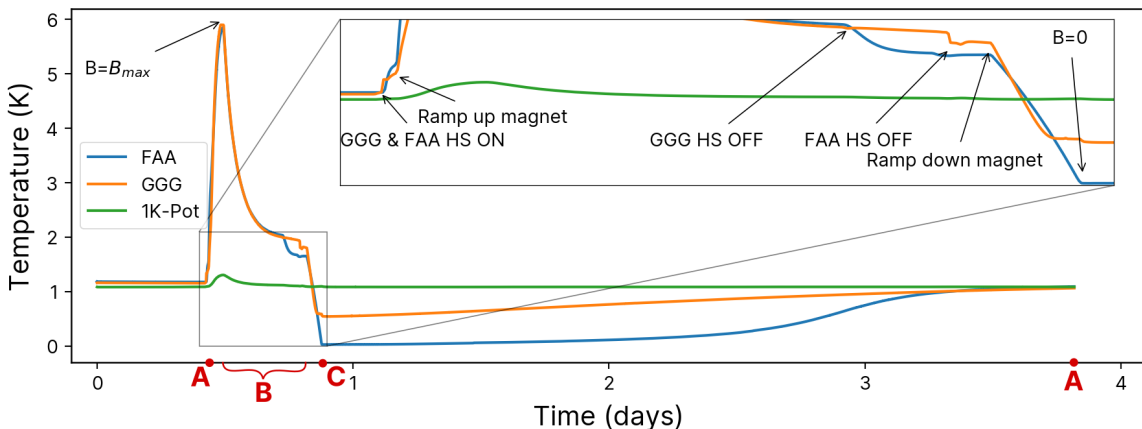


Figure 3.2: One full ADR cooling cycle, the steps A-C from figure 3.1 are labeled in red: First, the paramagnets are thermalized to the 1-K-pot by turning on the heatswitches. Then the ADR magnet is ramped to 6 T. The heated paramagnets FAA and GGG are still connected to the 1K-pot and therefore cool down after the magnet ramped up. Then the thermal connection to the 1K-pot is interrupted by turning off the heat-switches. Now ramping down the ADR magnet demagnetizes the thermally isolated paramagnets, which leads to a drop in temperature. GGG and FAA reach different minimal plateaus and gradually warm up to 1 K over roughly 3 days.

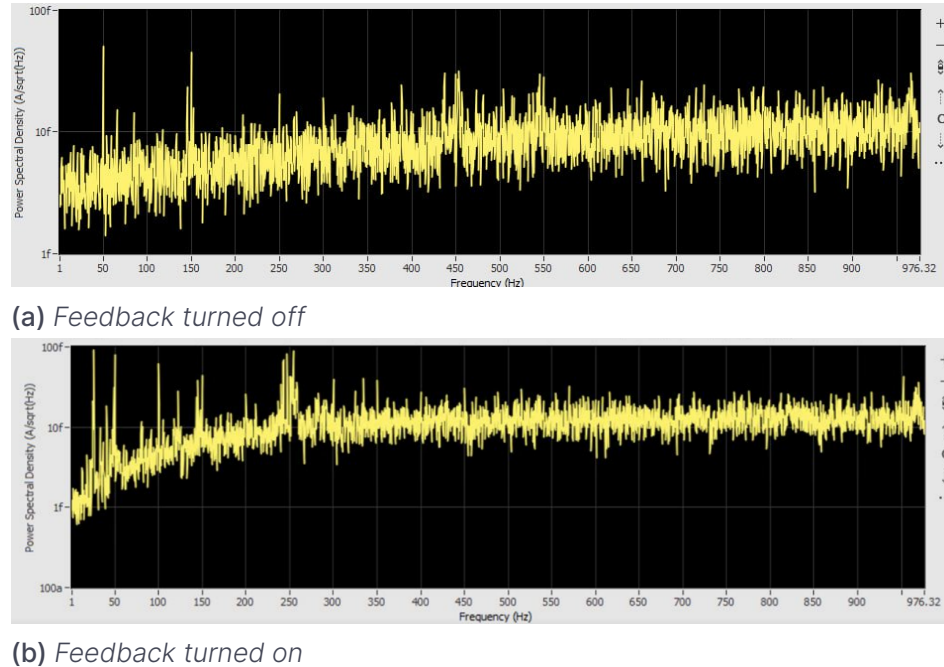


Figure 3.3: The noise of the STM with tip and sample being in contact at 1 K, $I = 100 \text{ pA}$ and $V = 10 \text{ mV}$ with feedback turned on and off, respectively. The visible reduction of noise for low frequencies in (b) is due to the operation of the feedback loop. The noise does not alter significantly for millikelvin temperatures.

power spectral density of the tunneling current with open feedback therefore stays well below $100 \text{ fA}/\sqrt{\text{Hz}}$ for frequencies below 1 kHz, as shown in figure 3.3.

The home-built STM has both z-coarse motion and xyz-scanning function combined in a single piezoceramic tube developed by mProbes [63]. This compact design further reduces mechanical noise.

Apart from the magnets that magnetize and demagnetize the ADR material, there is also a magnet that is used to apply an out-of-plane magnetic field of up to 8 T to the sample. Both magnets are fully immersed into liquid Helium and superconducting. By switching the sample magnet to the persistent mode, thus forming a closed superconducting loop, the supply current can be turned off to avoid electrical noise in the system.

3.2 Sample Preparation

The sample was prepared by thermal evaporation of the NTCDA molecules onto an Ag(111) crystal. The crystal was cleaned by repeated cycles of 1 keV Ar^+ sputtering and annealing at 500 °C at a chamber pressure of around $1 \times 10^{-10} \text{ mbar}$. In there, also the surface quality could be checked by LEED. The clean Ag(111) surface shows a sharp 1×1 pattern due to its six symmetry-equivalent domains, as can be seen in figure 3.4a.

The molecules then were evaporated from a custom-built Knudsen cell at

160 °C for 2 min onto the Ag(111) crystal at room temperature. The resulting LEED pattern shows an additional superstructure on top of the 1×1 pattern, which indicates the formation of a molecular monolayer, as can be seen in figure 3.4b. As discussed by Stahl et al. [64], this pattern can be observed for an NTCDA coverage ranging from 0.1 to 0.9 monolayers. The according matrix of the NTCDA superstructure is given by [65]

$$G = \begin{bmatrix} 4 & 0 \\ 3 & 6 \end{bmatrix}. \quad (3.1)$$

The high symmetry of the LEED patterns can be described with three rotational domains with a rectangular unit cell. The unit cell of one domain is shown in figure 3.4c, as obtained by Kilian et al. [66]. The quality of our LEED pattern is not sufficient to resolve the NTCDA unit cell. This is because the design of the manipulator in the preparation chamber limits the minimal distance between the sample and the LEED screen. In addition, this limiting structure is also believed to perturb the electric fields in vicinity of the sample, which can blur the LEED pattern.

For higher coverages, the arrangement of the molecules on the surface changes (i.e. the phase transitions from a *relaxed* to a *compressed* state) which results in a different superstructure [64]. To build a standing NTCDA molecule, it is necessary to have clean silver areas, therefore a coverage of < 1 monolayer is desired.

The sample was then cooled to -70 °C and transferred to the STM.

3.3 Molecular Manipulation

The manipulation of single molecules on surfaces is a key technique in STM experiments. It has already been described in detail how PTCDA molecules can be lifted from the surface [17, 67] or out of the monolayer [68]. An optimized procedure using virtual reality was also described [69].

The same procedure can be applied to extract an NTCDA molecule from inside an island or from the islands edge (see figure 3.5): In a first step the carboxylic oxygen, i.e. one of the corner oxygen atoms, is approached with the tip at low bias (1 mV) until the current jumps to several nA, signaling that a covalent bond has been established [16, 17]. Next, the tip is lifted and moved laterally over the diagonal of the molecule, such that the final position of the tip is above the diagonally opposite carboxylic oxygen. The path is sketched in figure 3.5b. At the end of this procedure, the current should be about 100 pA. If the molecule is inside the island, the tip then has to be retracted further until the single molecule is completely detached from the sample, i.e. the current dropped to zero. Now the molecule can be put down on a clear Ag terrace by applying a voltage pulse of around 2 V. An example for the extraction of molecules from a monolayer is shown in figure 3.6.

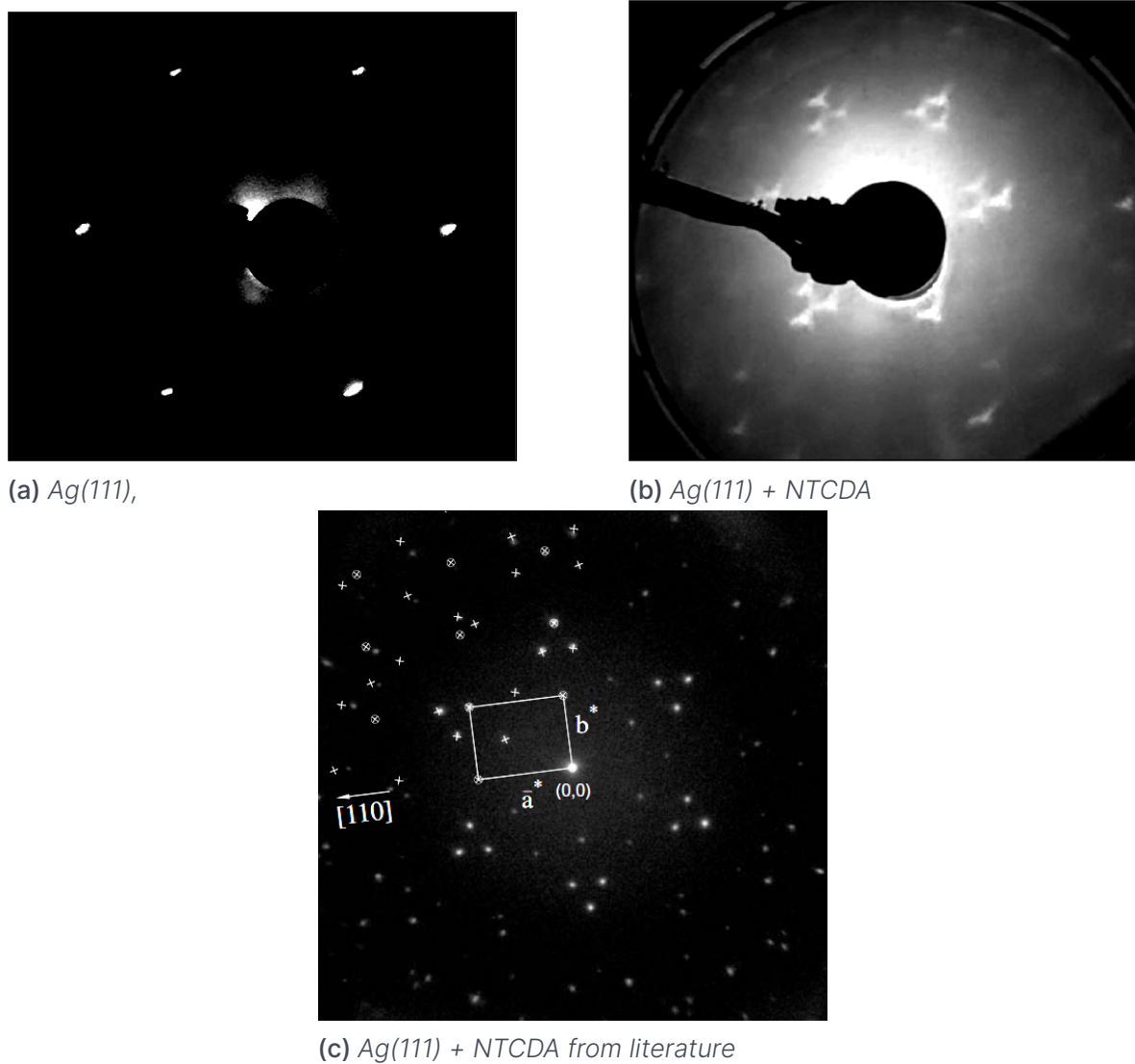


Figure 3.4: LEED images of Ag(111) right after the cleaning procedure (a) and after deposition of NTCDA (b). The 1×1 pattern is clearly visible in both images, but only in (a) with a superstructure, which indicates the formation of a molecular monolayer. The same LEED pattern in higher quality from literature [66] is shown in (c). The unit cell of one rotational domain is marked by the white rectangle.

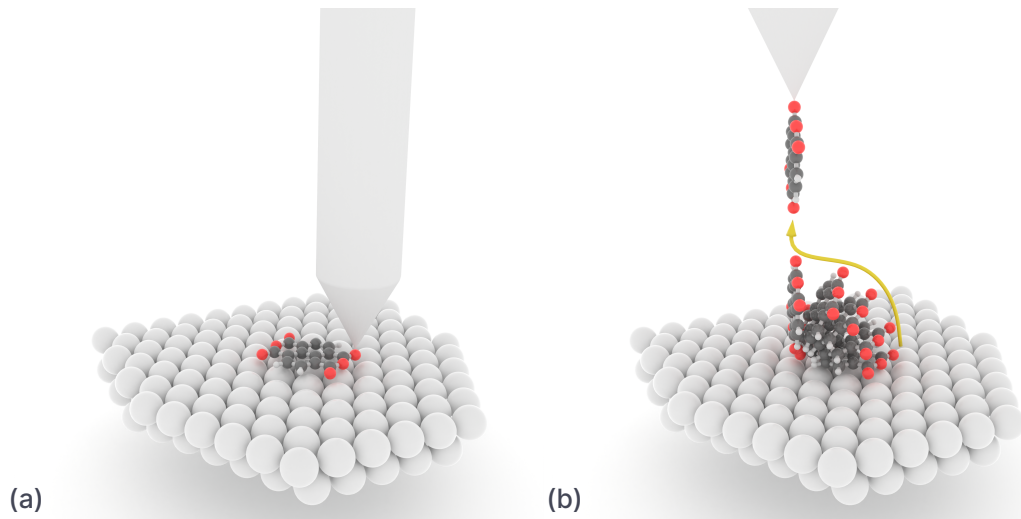


Figure 3.5: Lifting an NTCDA molecule from the surface. **(a)** First a carboxylic oxygen atom is approached by the tip, forming a covalent bond. **(b)** Then the molecule gets gradually rotated along its diagonal and is subsequently lifted vertically.

Experimentally it is easier to extract a molecule from the edge of an island (as in figure 3.7b). After having lifted the molecule into the vertical position, no further retraction is necessary, as the molecule can then be dragged away by moving the tip laterally over the surface with a speed of around 300 pm s^{-1} . With this technique, not only vacancies and small molecular islands can be created, but also standing molecules, as is described in [19]. The procedure works for PTCDA as well as NTCDA on Ag(111).

As a starting point, two Ag atoms are deposited in vicinity on an Ag terrace (see figure 3.7a). This is done by very shallow tip crashes (z -shift of -650 pm at $I = 100 \text{ pA}$ and $V = 100 \text{ mV}$ setpoint) at $V = 0$. After having picked up an NTCDA molecule from an island edge as described above, one can drag the molecule across the surface to one of these adatoms (feedback off, $I = 10 \text{ pA}$ and $V = 10 \text{ mV}$), whereupon the current suddenly increases. As the tip is moved further laterally, the current remains on the high level, implying that the adatom formed a bond to one of the carboxylic oxygen atoms at the bottom of the molecule and is now being dragged over the surface. When this structure is moved to the second Ag adatom, the second carboxylic oxygen usually attaches to it instantly, which can again be inferred by a sudden increase in current.

Retracting the tip some Å then breaks the tip-molecule bond, because the two identical Ag-O bonds on the surface are stronger. This leaves the NTCDA molecule standing on the two Ag adatoms, which can be checked by scanning the molecule in constant height at $1 \text{ pA} \lesssim I \gtrsim 2 \text{ pA}$ and $V = 50 \text{ mV}$. If the scan shows two lobes as in figure 3.9a, the molecule is standing upright on the surface [19]. The nodal line is oriented perpendicular to the molecular plane, as visualized in figure 3.9b.

To put the molecule in a horizontal configuration in a controlled way, the tip,

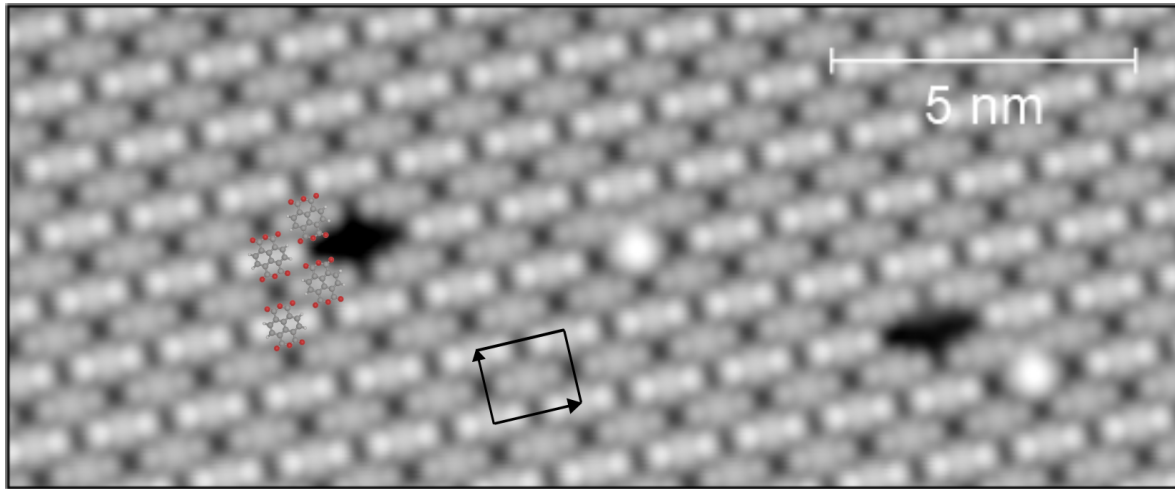


Figure 3.6: Extracted molecules (black holes) in a NTCDA monolayer. The orientation of the molecules is indicated by the overlayed NTCDA models. The unit cell is marked by the black rectangle.

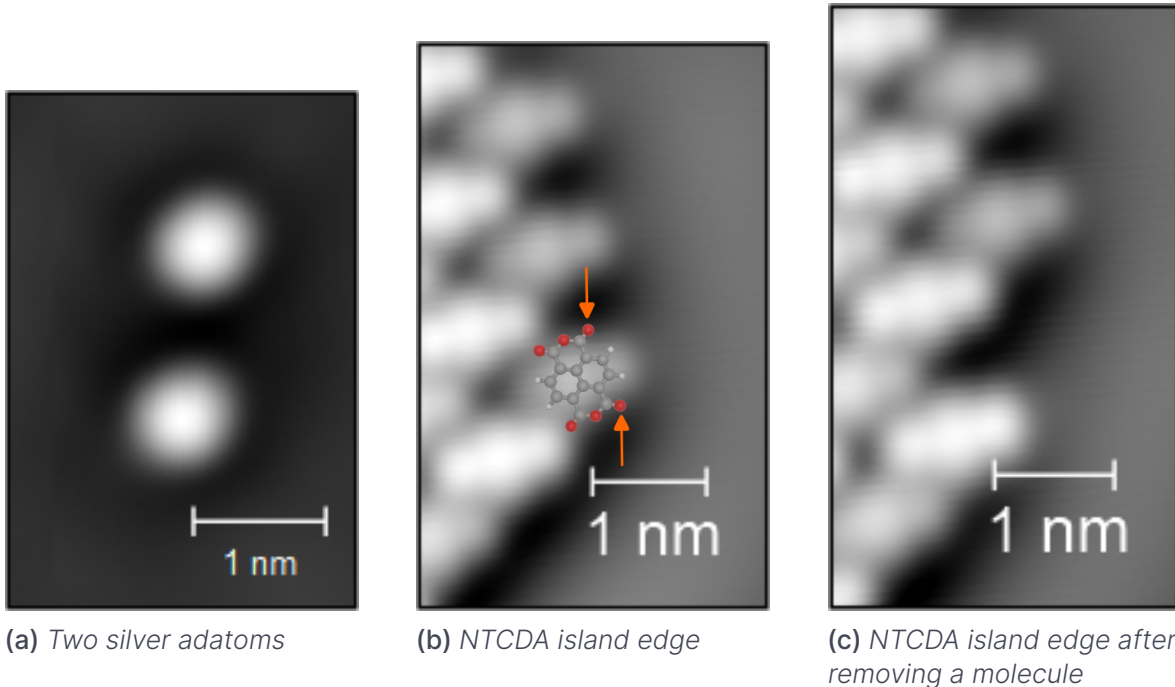


Figure 3.7: To construct a standing NTCDA molecule, a single molecule from an island edge has to be extracted and moved over two Ag adatoms. The orange arrows mark the position of the carboxylic oxygen atoms of the molecule that is moved.

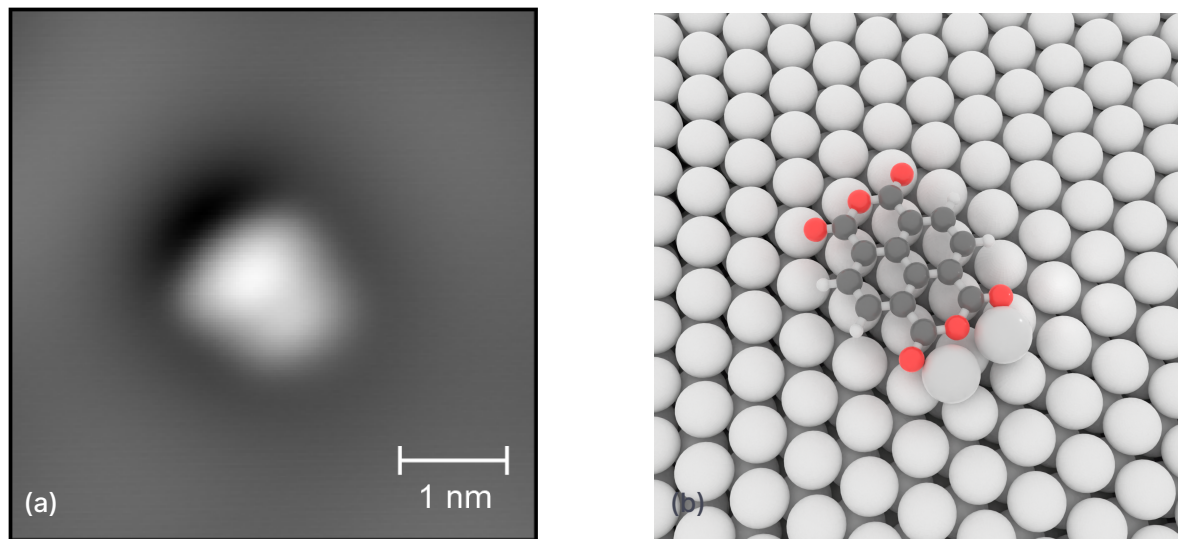


Figure 3.8: The nanostructure NTCDA+2Ag in its horizontal configuration. **(a)** Constant current image of the molecule. **(b)** Graphical visualization of the same structure.

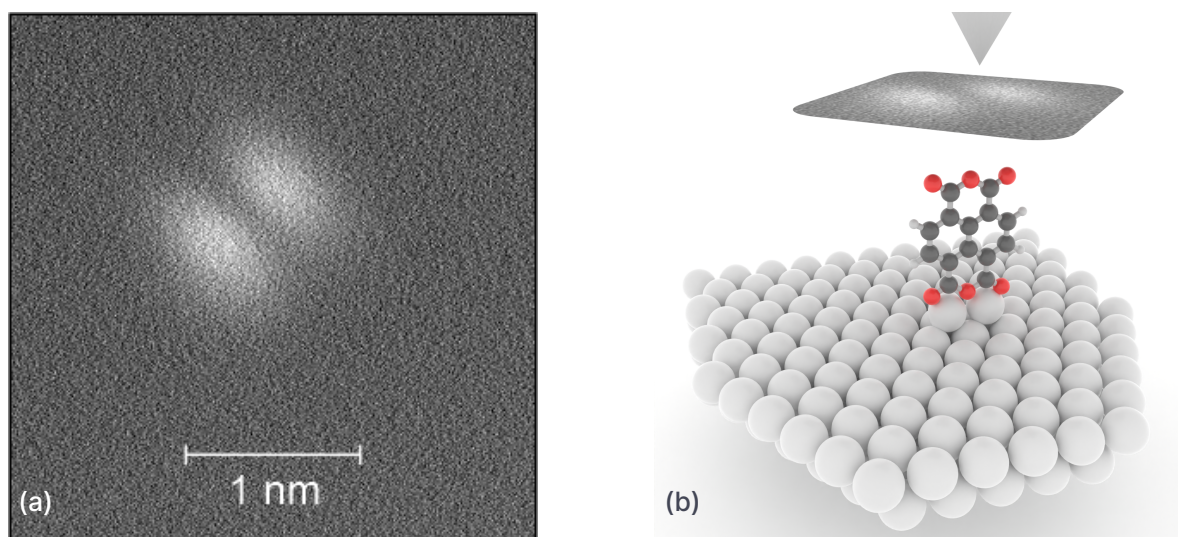


Figure 3.9: The nanostructure NTCDA+2Ag in its vertical configuration. **(a)** Constant height image of the molecule. **(b)** Graphical visualization of the structure, including the scan.

being in scanning conditions above the molecule, is moved laterally 40 Å away from the molecule. Then the applied bias voltage is increased to 1 V and the tip moved back to the molecule, which at this high voltage flips back to the surface, still being attached to the Ag dimer, see figure 3.8. From there it can be stood up again at will. This is done similarly to how the molecule is lifted from the surface: One of the two corner oxygen atoms that is not bound to the Ag adatoms is contacted with the tip. The lifting trajectory that follows is similar, only that the final lateral position is not above the diagonally opposite corner oxygen atom, but above the closer Ag adatom. Further retraction again breaks the tip-molecule bond and leaves the molecule standing.

The standing PTCDA was found to adsorb with its silver atoms in hollow sites of the Ag(111) surface [19]. If one of the adatom is assumed fixed in a hollow site, the other adatom can be located in 9 different sites, corresponding to rotations of the molecule. This was not investigated systematically for NTCDA, but is assumed to be the same as the constituents of the chemical bond are identical. The standing NTCDA could be rotated by moving over it laterally with $V = 50 \text{ mV}$ and $I > 2 \text{ pA}$.

3.4 Data Analysis

3.4.1 Spectrum Processing

The dI/dV spectra were recorded with Nanonis software in one or multiple sweeps, that were saved separately. Already during experiment close attention was paid to avoid piezoelectric creep in all dimensions by letting the piezo scanners relax for some hours after long-range movement (like tip approach or movement from tip preparation site) and also by adjusting the z-position during data acquisition depending on the current at the beginning of each sweep, trying to keep it constant. To combine the separate sweeps, a linear slope was additionally added to all sweeps but the first, such that the current at the beginning and at the end of each sweep was normed to the first sweep. To The dI/dV spectra are expressed in units of the conductance quantum $G_0 = \frac{2e^2}{h}$.

3.4.2 Spectrum Fitting

Fitting Kondo resonance line shapes in scanning tunneling spectroscopy needs a cautious treatment to extract real fit parameters, as is discussed in detail by Gruber et al. [50]. The internal spectral shape is changed by the modulation amplitude of the lock-in amplifier as well as by the temperature of the STM junction. Both influences result in a convolution of the natural line width with a particular broadening function. The modulation broadening can be described as [50]

$$\chi_{\text{Lock-in}}(V) = \begin{cases} \frac{2\sqrt{V_m^2 - V^2}}{\pi V_m^2}, & \text{if } |V| \leq V_m \\ 0, & \text{otherwise.} \end{cases}$$

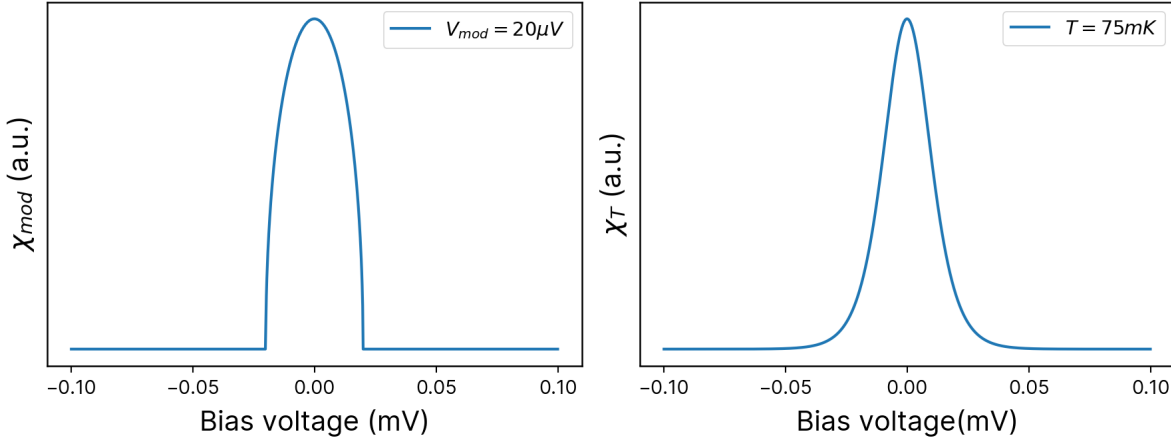


Figure 3.10: Broadening functions for the lock-in modulation (left) and the temperature (right) for the values mentioned in the text.

The temperature broadening is given by the derivative of the Fermi-Dirac distribution [50]

$$\chi_T(V) = \frac{k_B}{4k_B T \cosh^2\left(\frac{eV}{2k_B T}\right)}.$$

The total broadening function then reads $f_{Kondo}(p) * \chi_{Lock-in} * \chi_T$, where $f_{Kondo}(p)$ is the natural Kondo resonance line shape with parameters p . The two broadening functions are displayed in figure 3.10. The temperature broadening can obviously only be kept low by operating at low temperatures, which is why we measured as soon as the ADR-cycle reached its minimal temperature. As noted above, the tip temperature is $T_{tip} = T_{ADR} + 45\text{ mK}$, with the minimal value $T_{ADR} = 30\text{ mK}$ used in figure 3.10. The modulation amplitude, on the other hand, is an instrumental parameter that can be adjusted. The optimal value is a compromise between a high signal-to-noise ratio and a low broadening. In our case, $V_m = 20\text{ }\mu\text{V}$ was used, which is a good compromise for the low temperatures of operation, as can be seen by comparing the two broadening functions. More precisely, the full-width at half-maximum (FWHM) of χ_{mod} is $1.7V_m$ and the FWHM of χ_T is $3.5k_B T$. Therefore, $V_m < 2.06k_B T$ is a reasonable choice to which was mostly followed during the experiments.

Very recently, an analytical expression for the temperature broadened Frota function was derived [44]. The resulting expression is based on the Hurwitz ζ -function. Despite its complex analytical form, the fitting procedure is simple due to the provided python package [70]. We tested the new procedure with our data and found good agreement with our fitting results.

4. Results

In the following, the results characterizing the Kondo effect in the standing NTCDA are presented. All measurements were conducted with the tip residing above one of the lobes of the standing molecule, as depicted in figure 4.2a.

4.1 Spin g-factor

A first step to characterize the standing NTCDA molecule is to determine the electronic configuration. This is done by extracting the spin g-factor. In high magnetic fields, the inelastic spin-flip excitations result in a gap symmetric around zero bias as mentioned in section 2.1.2. The width Δ of the gap is described by

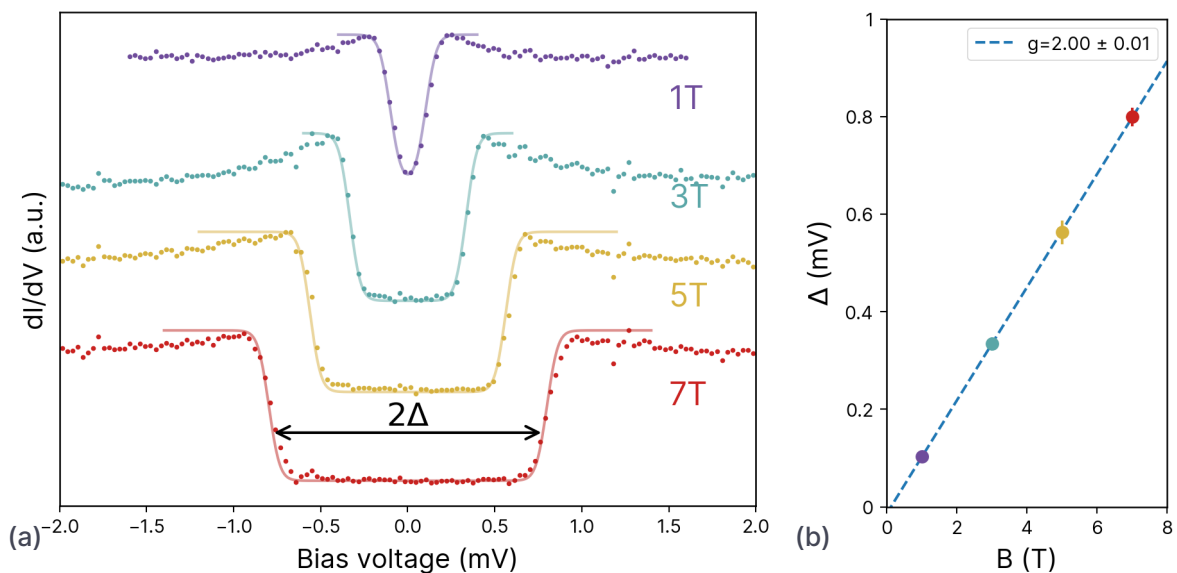


Figure 4.1: (a) Spectroscopy on the standing molecule with different out-of-plane magnetic fields. The inelastic spin-flip excitations above the energy Δ appear as two steps in the dI/dV spectrum, that shift to higher energies with increasing magnetic fields according to the Zeeman effect. The solid lines are fits of a broadened rectangular gap (see section 3.4.2). (b) The gap width Δ as extracted from (a). The linear fit $\Delta = g\mu_B B$ agrees well with the expected $g = 2$ for a free electron. The spectra were obtained by averaging 3 sweeps with a setpoint $I = 25$ pA, $V_{mod} = 50$ μ V at a temperature $T = 40$ mK.

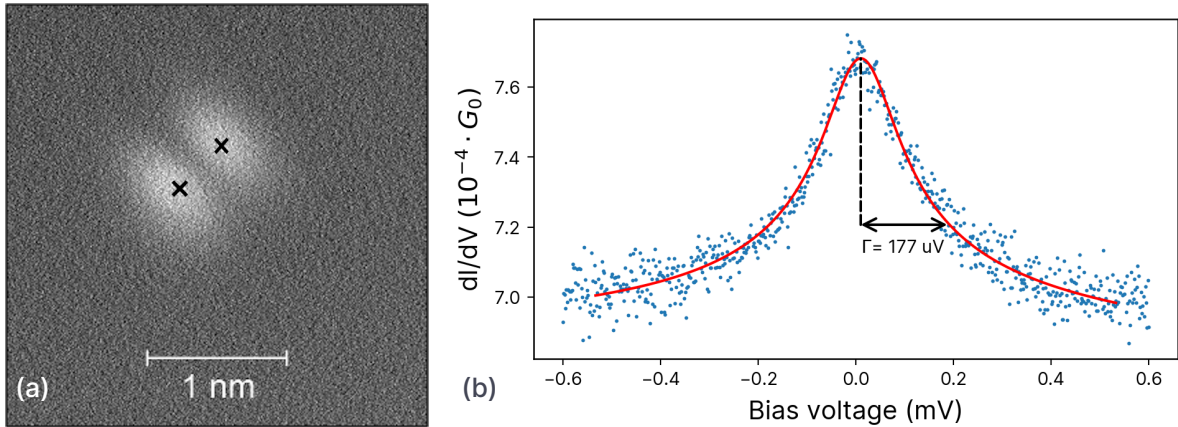


Figure 4.2: (a) The measurements on the standing NTCDA were done on the lobes where the highest current was measured. Two exemplary measurement positions are marked with black crosses. (b) A zero bias peak appears in the dI/dV spectrum above the standing NTCDA at $T = 40 \text{ mK}$ and $B = 0 \text{ T}$. Red line is the fit with the Frota function. Measured by averaging 8 sweeps and an initial setpoint $I = 32 \text{ pA}$ and $V = 1 \text{ mV}$, $V_{mod} = 20 \mu\text{V}$.

the Zeeman effect $\Delta = g\mu_B B$, where g is the g-factor, μ_B is the Bohr magneton and B is the magnetic field. The g-factor can be obtained by fitting the gap width Δ as a function of magnetic field B (see figure 4.1b). The gap width is extracted by fitting a rectangular gap function that was broadened as described in section 3.4.2 (see figure 4.1a). The linear fit $g = 2.00 \pm 0.01$ is in very good agreement with the expected $g = 2$ for a free electron.

4.2 Magnetic Splitting of the Kondo Peak

Yet, spectroscopic measurements of the system at zero magnetic field and at millikelvin temperatures refute the assumption of a free spin: Under these conditions, a clear zero bias peak is visible (see figure 4.2b). It is reasonable to assume its origin to be the Kondo effect, because the standing molecule was identified as a spin- $\frac{1}{2}$ magnetic impurity on a metallic surface. This would imply that the single spin is not actually free but entangled with the electron bath of the metal surface. That interpretation is corroborated by spectroscopic measurements at low magnetic fields (see figure 4.3a): A critical magnetic field B_C has to be applied for a gap to start forming [20]. This is a clear indication of the Kondo effect, as the correlation energy due to the formation of a Kondo singlet has to be exceeded [71]. In order to quantify the coupling strength of the impurity spin to the silver electron bath, B_C is extrapolated to then derive the Kondo temperature T_K of the system. Identifying the dips as split Kondo peaks, it should be noted that theoretically the peaks for $B \geq B_C$ are spin up and spin down impurity spectral densities [71], that are not described by a rectangular dip, which is physically sensible for larger magnetic fields. In order to account for both limiting cases, two different methods are applied to extract the splitting

gap width Δ , as shown in figure 4.3b for different magnetic fields.

The first approach is to again fit temperature- and modulation-broadened rectangular gap functions to the spectra (red data), the gap width and depth being fit parameters. For the other method the dI/dV was smoothed using a second-order Savitzky-Golay-filter and subsequently the dI^2/dV^2 was calculated numerically (blue data in figure 4.3b). The position of the inflection points in the dI/dV spectra can now be obtained by fitting the peak location in the dI^2/dV^2 with Gaussian functions. The resulting gap widths Δ are displayed in figure 4.4. The fitted rectangular gaps widths increase linearly with increasing magnetic field. The Δ obtained from the second method on the other hand first broadens quickly to then remain roughly constant. The critical magnetic field B_C can then be extracted by a linear extrapolation to $\Delta = 0$. Both approaches give similar values: 42 ± 9 mT with the first and 39 ± 8 mT with the second method. Note that the large relative uncertainties stem from the weakly pronounced dip shape for $B \geq B_C$. We also mention that these fits should not be used to deduce the g-factor due to the superposition of peak and step-structures [48].

The averaged $B_C = 40 \pm 6$ mT can now be used to determine the Kondo temperature with the relation [71]

$$k_B T_K = 2g\mu_B B_C. \quad (4.1)$$

This yields $T_K = 109 \pm 16$ mK. We remark that equation (4.1) is a $T = 0$ result and precise for $T < 0.25T_K$ [71], which is not the case for our measurement at $T = 40$ mK by a small margin. Therefore, T_K can be expected to be at the lower error bound of the estimate.

This first estimate of T_K is remarkably low for adsorbates on metal surfaces, in fact the lowest ever measured, to our knowledge. Lower Kondo temperatures have only been obtained in experiments with lithographically defined mesoscopic quantum dots [47, 72].

To obtain another estimate of T_K , the Kondo peak was measured for a large temperature range from $T = 40$ mK to 760 mK (see figure 4.5a). T_K can be extracted from the temperature dependence of the zero-bias conductance with an empirical fit function [73], yet our measurement series is not precise enough for this procedure. In the experimental temperature range of 800 mK, the maximal difference of the background subtracted zero bias peaks is only $5 \times 10^{-5} G_0$, such that already small measurement perturbations induce big relative errors. The spectra were obtained over a period of 2.5 days with repeated approach to and retraction from the molecule, in order to avoid tip-molecule interaction between the measurements. Therefore, the lateral position relative to the molecule can vary by some Å for each approach, which would result in a different tip-molecule stabilizing distance and consequently also a different conductance. This might explain why the change of the Kondo peak height is not resolved with the needed precision.

As the width of the Kondo peak does not depend on the absolute peak height, this parameter can be utilized to extract the Kondo temperature.

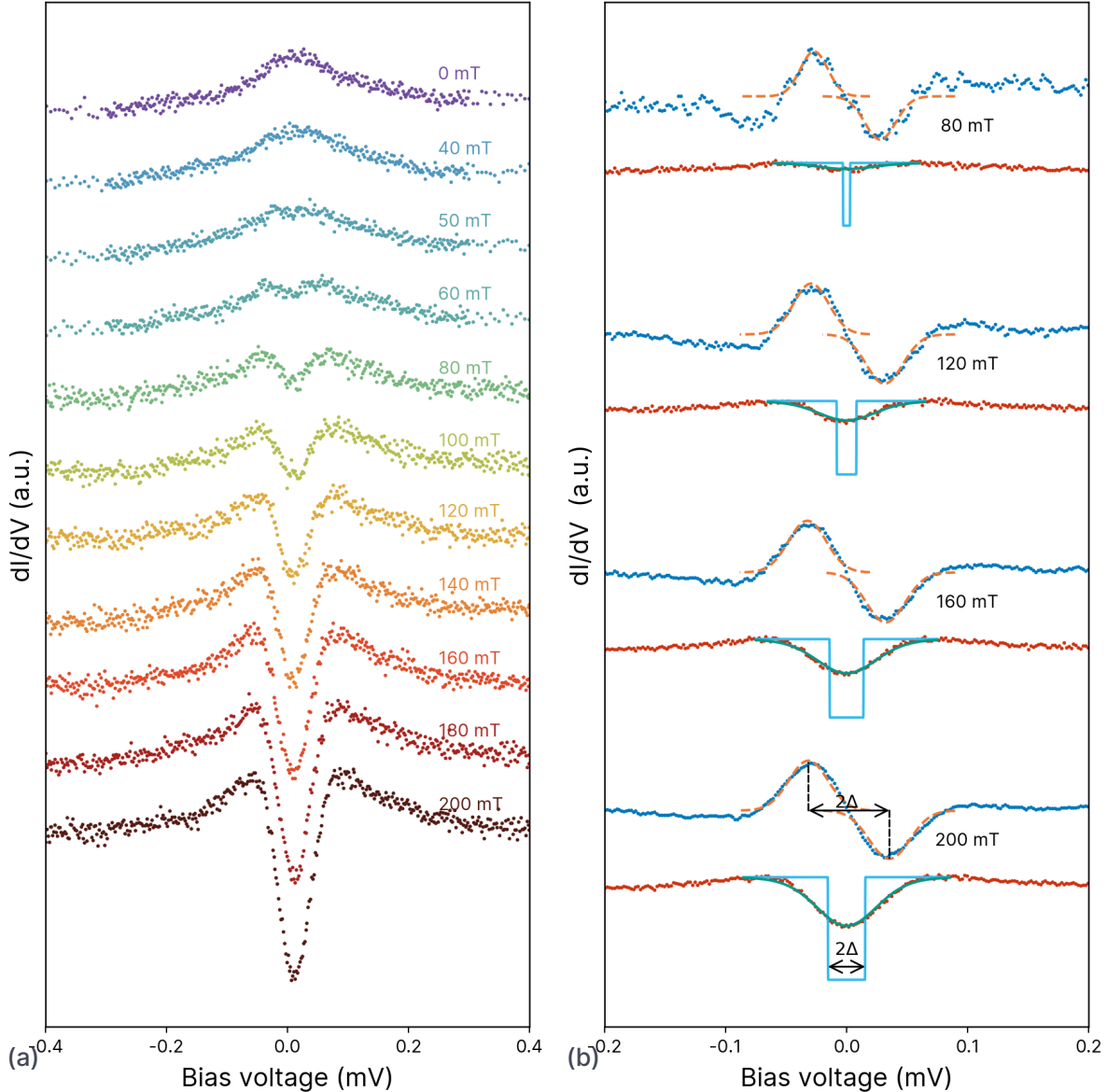


Figure 4.3: (a) dI/dV spectra above the standing molecule with increasing magnetic field. The Kondo peak at 0 mT gets split into two peaks for $B \geq 40$ mT. (b) Exemplary demonstrations of two methods to extract the gap widths for chosen spectra in (b): i) The gap (red data) is fitted with a rectangular gap function, that was broadened according to section 3.4.2. The gap width and depth were fit parameters. ii) The spectra is smoothed and numerically differentiated (blue data). Then the peak position are fitted with Gaussians. For clarity, the spectra were shifted vertically. The spectra were obtained by averaging 4 sweeps with a setpoint $I = 32$ pA, $V_{mod} = 20$ μ V at a temperature $T = 30$ mK to 40 mK.

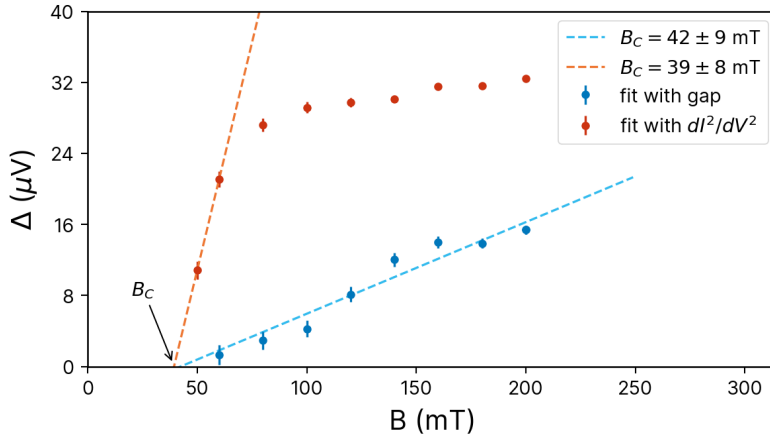


Figure 4.4: The gap widths extracted like in figure 4.3b as a function of the magnetic field. The fitted gap width (blue) and the dI^2/dV^2 method (red) are linearly fitted, for the latter only the steep ascent. The crossing of the fit with the B -axis defines $B_C = 40 \pm 6$ mT.

4.3 Line Width Evolution of the Kondo Peak

The halfwidth (from now on *width*) of the Kondo peak is obtained by fitting a Frota function with a linear background to the spectra. Before performing the least-square fit, the Frota function is broadened numerically with temperature and modulation, as explained above. This broadening is only then not performed if explicitly mentioned in the following.

A first guess of the Kondo temperature is obtained by fitting the Kondo peak at the lowest temperature $T = 30$ mK (see figure 4.2b). The width at 0 K, the *intrinsic width* Γ_0 , then defines the Kondo temperature $k_B T_K = \Gamma_0$. If we assume the width at 30 mK to be similar to the 0 K value, the extracted width $\Gamma(30\text{ mK}) = 172 \pm 5$ μV yields $T_K = 2000 \pm 80$ mK. Yet, as the width increases with rising temperature [43, 52], it is not a priori clear that $\Gamma(30\text{ mK}) \approx \Gamma_0$.

A more precise estimate can be obtained by analyzing the width evolution for different temperatures. For this purpose the Kondo peak was measured and fitted in a temperature series, see figure 4.5a. Two fits are compared: The function proposed by Nagaoka et al. [52] has been used extensively in the literature in the last two decades:

$$\Gamma(T) = \frac{1}{2} \sqrt{(\alpha k_B T)^2 + (2k_B T_K)^2} \quad (4.2)$$

We use the theoretically predicted $\alpha = 2\pi$. Often α is left as a fit parameter for a more accurate fit, but it was shown that then the function is so tunable that its fit is not a reliable proof for a Kondo system anymore [44].

In an effort to tackle this lack of understanding, Jacob [43] recently derived a description of the line width from a novel theoretical Ansatz for the renormalized self-energy that extends the temperature and energy range beyond the Fermi

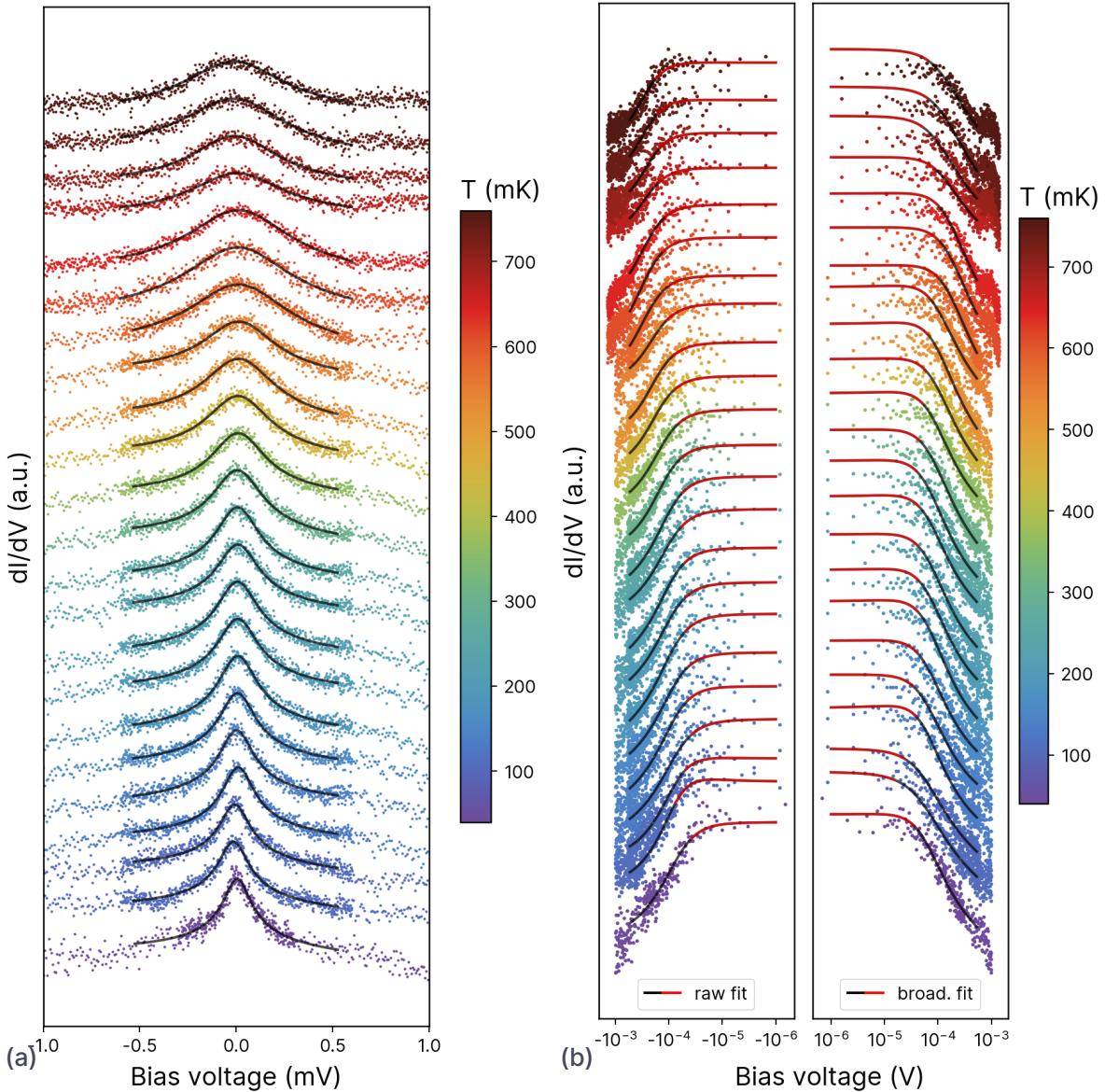


Figure 4.5: (a) dl/dV spectra of the Kondo resonance above the standing molecule for different temperatures and $B = 0$. A frota function with a linear background was fitted to the spectra (black line). (b) Logarithmic view of (a). The simple frota fits are shown in the left panel, whereas the fits in the right are deconvoluted from the temperature broadening and therefore show a more pronounced line shape. The red lines highlight the segments of the Frota fits that deviate no more than 0.1 % from the according maximum value. The dl/dV was averaged in 2-6 sweeps with a current $I = 42$ pA at $V = 1$ mV, $V_{mod} = 20$ μ V.

liquid regime:

$$\Gamma(T) = \Delta_k \sqrt{a + b \sqrt{1 + \left(\frac{\tau}{\Delta_k}\right)^2} + c \left(\frac{\tau}{\Delta_k}\right)^2}, \quad (4.3)$$

where $a = 1 + \sqrt{3}$, $b = 2 + \sqrt{3}$, $c = \sqrt{3}/2$ are constants, $\tau = \pi k_B T$ is the temperature parameter and Δ_k is related to the Kondo temperature as $k_B T_K = 2.542 \Delta_k$. In the following, the standard approach in equation (4.2) is compared with the very recent proposal in equation (4.3).

The experimental line widths $\Gamma(T)$ together with the fits are displayed in figure 4.6a. After the 16th spectroscopic measurement the tip contacted the standing molecule, resulting in a sudden jump in conductance. A current height scan (as in figure 3.9a) above the molecule subsequently revealed a change in the junction. Probably the tip apex configuration changed, maybe also the position of the molecule-dimer nanostructure on Ag(111). The structure is stable for two different binding configurations of the dimer on the surface [19], which could lead to different molecule-surface hybridization. Therefore, the measurements that followed were not included in our analysis.

Evidently, the evolution is better captured by equation (4.3).

The good agreement reinforces the assumption, that the zero bias peak indeed is the Kondo resonance. Inspecting the fit from equation (4.3) it is evident that the width at the lowest measured temperature has indeed reached the 0 K value. Therefore, the obtained $T_K = 1.78 \pm 0.20$ K is close to the result of the single fit.

As equation (4.3) is an exact analytical function only dependent on the known experimental temperature, and as it captures the width evolution very well, the T_K can also be extracted for a single Kondo peak at any finite temperature. To this end, equation (4.3) is rewritten to obtain the intrinsic Kondo line width [44]:

$$\Gamma_0 = 2.542 \sqrt{\sqrt{\frac{1}{3} \Gamma^4 + \frac{1}{3} \tau^2 \Gamma^2 + \alpha \tau^4} - \beta \tau^2 - \gamma \Gamma^2} \quad (4.4)$$

We use this method to estimate T_K at every temperature individually, as shown in figure 4.6b. The individual estimates agree very well with the ensemble result from equation (4.3), the red horizontal line. Evidently, the individual treatment cannot proof the Kondo nature of the peak, yet if this is known, it is a fast method to determine the Kondo temperature.

It is noted that for this analysis the tip temperature is an important parameter. The tip temperature is used for the broadening of the Frota function before fitting it to the spectra. Neglecting this results in a large overestimation of the width and therefore also of T_K , see figure 4.6c. This effect increases for rising temperatures. For the tip temperature we used the value $T_{tip} = T_{ADR} + 45$ mK as mentioned above.

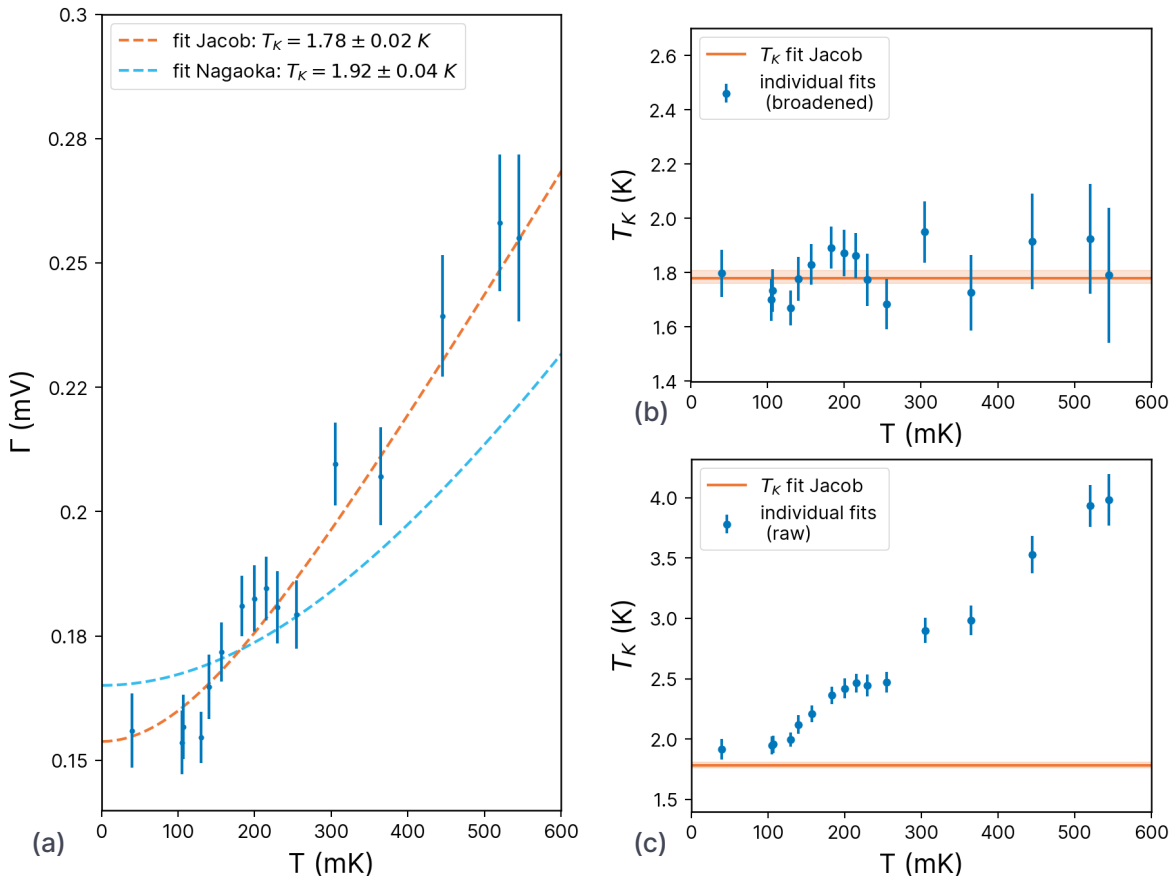


Figure 4.6: Inferring T_K from the peak widths in 4.5a. (a) The ensemble fits with equation (4.3) and equation (4.2). The fitted T_K are shown in the legend. (b) Individual fits with equation (4.4), compared to the ensemble fit T_K from (a). (c) Same as (b) but without convolution of the fitted Frota function due to Fermi broadening.

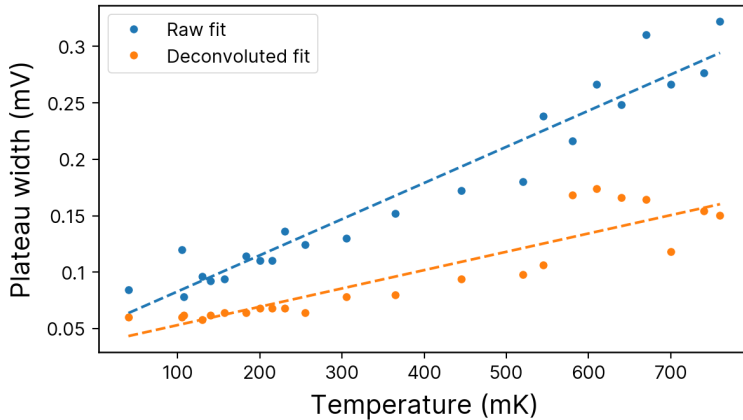


Figure 4.7: The widths of the plateaus from figure 4.5b plotted against the temperature for the raw (blue) and the deconvoluted fits (orange). The dashed lines are linear fits.

4.4 Temperature evolution of Kondo peak sharpness

The estimates of T_K obtained from the critical field and from the peak width differ substantially. Yet, they are both larger than our lowest experimental temperature $T \approx 30$ mK. This and the fact that a finite magnetic field is needed to split the Kondo peak is direct evidence that the system is not in the weak coupling regime, where other fitting functions were needed for the line shape but also for the width evolution [23, 48].

This is also reflected in the sharpness of the peak. As investigated by Yong-hui Zhang et al. [74], a strong linear dependence of the peak sharpness with decreasing temperature indicates a weak coupling Kondo system. The sharpness of the dI/dV curve can be identified - when plotting the bias axis on a logarithmic scale - as the width of the plateau around the peak. For our data this view is shown in figure 4.5b. On the left side, the dI/dV of the negative bias is plotted on a logarithmic scale together with a fitted frota function. It is visible that the fit is good also for very small bias voltages ($V < 100$ μ V), which justifies to solely analyze the fits. We define the plateau around the peak as all fit values that deviate no more than 0.1 % from the fitted peak intensity. This plateau is plotted in red for every fit. It is clearly visible that the width of the plateau increases with increasing temperature. Here again, one has to pay attention to the broadening due to temperature, which increases during the measurement series more than an order of magnitude. The deconvoluted fit, i.e. the actual frota function before the convolution with the derivative of the Fermi distribution, is shown in the right in figure 4.5b, again with the plateau marked in red. The evolution of the plateau width analyzed for both negative and positive bias is compared in figure 4.7. The temperature corrected width roughly doubles from $T = 30$ mK to $T = 760$ mK. This is significantly less than the increase of width of 150 % during a doubling of temperature which was observed by Zhang et al. [74]. Therefore, it can be taken as further evidence that the impurity spin at low temperature is not in the weak

coupling regime.

For temperatures $T > 550$ mK the evolution of the plateau width starts deviating for both the raw and the deconvoluted fit in figure 4.7. This cannot be clearly attributed to a change of the coupling strength, as the change of configuration due to tip-molecule interaction mentioned above also occurred at this temperature.

To investigate the crossover more carefully, measurements were done with the system at high magnetic fields, as described in the next section.

4.5 High Magnetic Field: Visualizing the Crossover

The weak coupling regime can be simulated well by using the perturbative Anderson-Appelbaum model mentioned in section 2.2. The physical crossover from the weakly to the strongly coupled Kondo regime can be directly observed as this approach breaks down for the strong interaction leading to a gradual change of the fit parameters [20].

This approach treats the tunneling as the scattering event of an incoming electron with the localized spin system up to third order in the exchange interaction J . It yields the spectral function of the Kondo peak also with magnetic field present. A detailed description can be found in ref [48].

Extracting J could be useful for further computations with the Anderson model, but as $J\rho - \rho$ being the density of states (DOS) of the sample at the Fermi energy - is a combined fit parameter, this is not possible. Therefore, the application of this model solely serves to obtain a further estimate for the Kondo temperature - the temperature where the crossover from the weakly to the strongly coupled regime occurs.

For the model to be applicable, the magnetic impurity has to be coupled much stronger to one electrode (here the sample), such that the spins are left in thermal equilibrium with the substrate. The latter is fulfilled by applying currents in the pA-range, such that it only probes the system but does not drive it out of equilibrium. As our system is not in the weak coupling regime, it has to be perturbed by applying a high magnetic field $B = 2$ T in order to reside in the high-field regime ($B \geq k_B T_K$).

We perform a least-square fit of the model to the temperature series of the split Kondo peak at $B = 2$ T. The spectra with the according fitted function are displayed in figure 4.8.

Whereas most parameters do not show any particular temperature dependence, the evolution of $J\rho$ and the g -factor follows a clear trend, as shown in figure 4.9. $|J\rho|$ is constant for $T < 600$ mK but then significantly decreases to stabilize again on a constant level. The absolute value of $J\rho$ is a measure for the coupling strength of the impurity spin to the substrate [48]. Therefore, the increase of $|J\rho|$ for lower temperature indicates an increased coupling to the substrate - the crossover to the strong coupling regime. At 0 T a divergence of

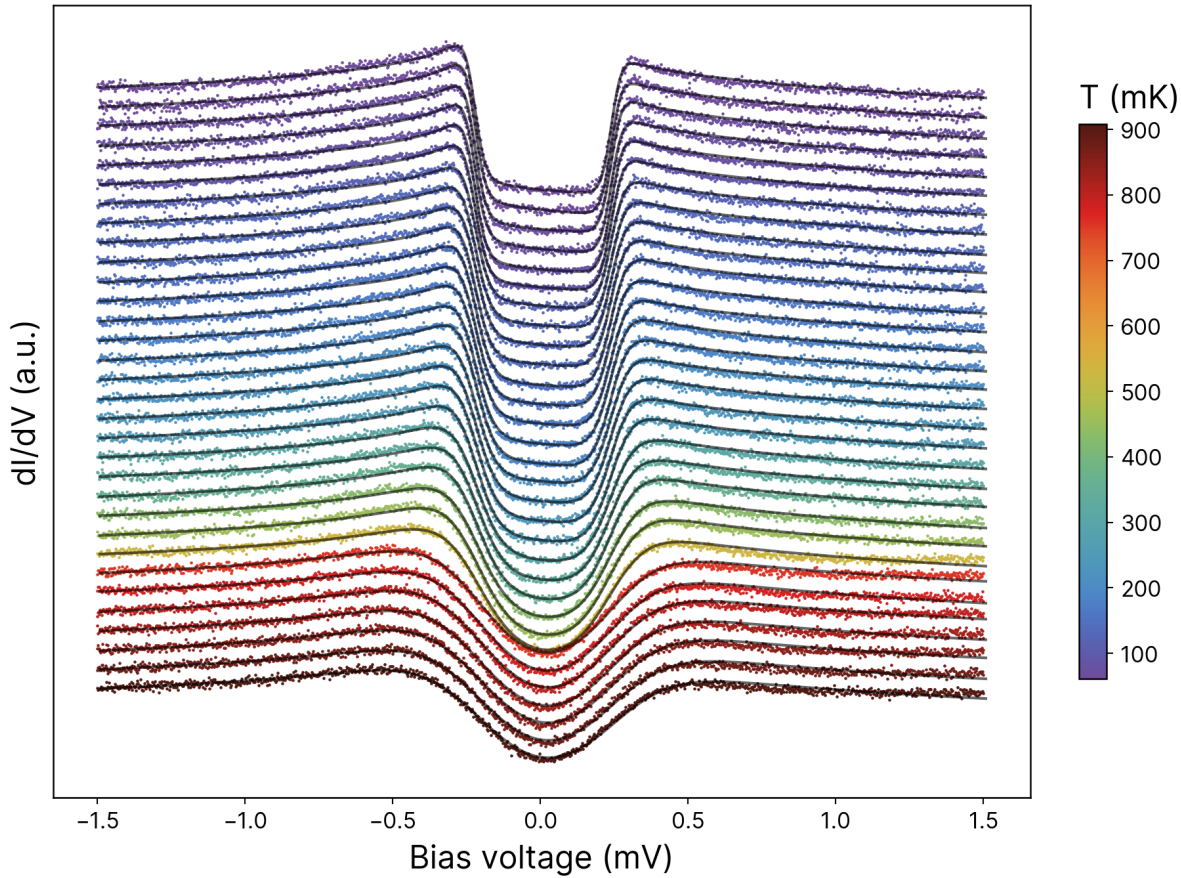


Figure 4.8: Spectra above the standing NTCDA molecule with a 2 T out-of-plane magnetic field for different temperatures. The solid lines are fits of the perturbative Anderson-Appelbaum model [48]. The spectra were obtained by averaging 4 sweeps with a setpoint $I = 50 \text{ pA}$, $V_{mod} = 20 \mu\text{V}$.

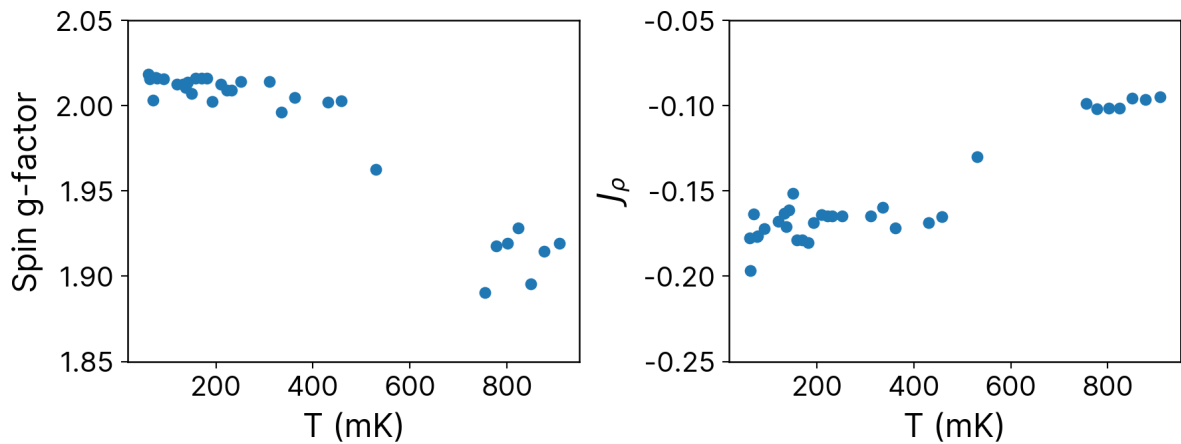


Figure 4.9: Spin g-factor and J_ρ as extracted from the fits in figure 4.8. The vertical dashed lines refer to the Kondo temperature obtained by the width Γ of the Kondo peak.

$J\rho$ would be expected as the impurity spin crosses over to a singlet state. The high field $B = 2$ T suppresses the formation of the singlet state.

The fitted g-factor also jumps from a constant value to a higher plateau upon falling below ~ 600 mK. This behavior can be rationalized by energy renormalization [75]: due to the coupling of the localized spin with the conduction electrons and their polarization by the magnetic field, the effective g-factor will be modified compared to the value for the free spin. Using this effect together with the previously obtained $g = 2$, another estimate for $J\rho(T)$ can be obtained [19, 74]. The resulting trend agrees well with our fits, even though the absolute values are shifted.

We note that the crossover temperature of around 600 mK is between our previous estimates of T_K . As no clear theoretical description of the crossover temperature exists, a precise value for T_K should not be extracted from this measurement.

4.6 Differences in the Kondo Temperature

The discrepancy between the Kondo temperature obtained from the critical magnetic field and the width of the Kondo peak is not uncommon, yet no fully persuasive explanation has been found yet. In the preceding investigation of the Kondo effect on the standing PTCDA molecule, the two values were different by a factor of four [20]. In this work the factor is even higher, around 17.

It has been argued that obtaining T_K from the resonance width can give unreliable results, depending on the system characteristics [76]. Using numerical renormalization group calculations it was shown that depending on the simulation parameters the obtained T_K varies in relation to other ways to determine T_K [76]. More precisely, an adjustment of the coulomb repulsion U in the impurity state by 20 % resulted in a change of T_K by 20 % in relation to the other spectroscopic footprints of T_K . Therefore, this approach is not a universal measure and depends on the particle-hole symmetry breaking of the system. As an experimental technique, the height of the peak at zero bias is more robust because no current flows and high-energy excitations and nonequilibrium ef-

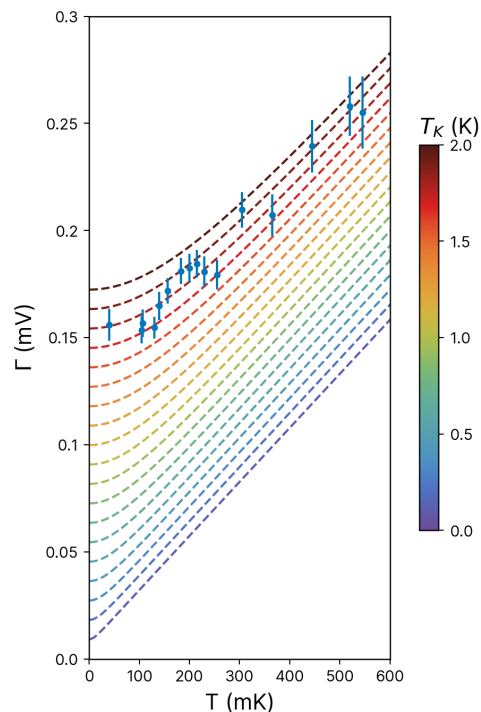


Figure 4.10: $\Gamma(T)$ from figure 4.6 and equation (4.3) with T_K from 0 K to 2 K. If all $\Gamma(T)$ are shifted vertically by the same amount, the function can still fit it well with a different T_K , as only the data point for the lowest temperature deviates from the linear trend.

fектs are thereby avoided [76]. Furthermore, it is noted that an absolute shift of the peak widths measured in the temperature series would still provide a good fit to equation (4.3), as shown in figure 4.10. Such a shift could occur through systematic broadening like a constant offset in temperature or instrumental noise. An erroneous derivation of the halfwidth could have the same effect: The small voltage range in figure 4.5a does not allow for a precise determination of the background, which can lead to a wrong halfwidth (at half maximum). Therefore, the good fit obtained verifies the Kondo nature of the peak, but is not a good measure for T_K .

This reasoning clearly restricts the accuracy of the width approach. On the other hand, applying magnetic fields to split the Kondo peak has been used successfully to infer a qualitative estimate of T_K [23, 77], but to our knowledge not quantitatively apart from ref. [20]. It should be noted that the measurements with magnetic field can be performed within a few hours in a small temperature range of about 10 mK and that between the measurements, the tip does not need to be retracted more than 1 nm. This results in a very controlled measurement series.

Apart from the drawbacks caused by the measurement duration and the increased tip movement already mentioned above, the temperature series that were performed for the width analysis also rely on a good knowledge of the sample temperature. As will be shown in the next section, the sample temperature is not straightforward to determine.

4.7 Junction Temperature

It has been shown that the temperature of the tip of the Jülich Quantum Microscope 1.0 for $T < 1\text{K}$ can be approximated by $T + 45\text{ mK}$, where T is the temperature read out by the sensor closest to the STM junction [61]. As the standing molecule is directly thermalized to the sample, a precise estimate of the sample temperature is evidently of interest. This can be done by analyzing the width of the spin IETS steps that were measured for 2 T and 4 T (see section 4.5).

Different broadening mechanisms are at play here: modulation amplitude of the lock-in amplifier, the lifetime of the excited spin state and - most importantly - the temperature of the tip and the sample. Usual spectra have to be deconvoluted - i.e. the fitting function have to be convoluted - once with the temperature broadening as most electrons tunnel from one Fermi edge to empty states (see figure 2.2). Yet for inelastic tunneling the electrons tunnel from the Fermi edge of the sample to the Fermi edge of the tip (or vice versa), as visualized in figure 2.5a. Therefore, the temperature broadening has to be deconvoluted twice [35].

We fit the spin IETS spectra at 2 and at 4 T with a simple rectangular gap function that is broadened by the modulation amplitude and by two independent temperature smearings, one for the tip and one for the sample. As the temperature of the tip T_{tip} is known and therefore one of the Fermi broaden-

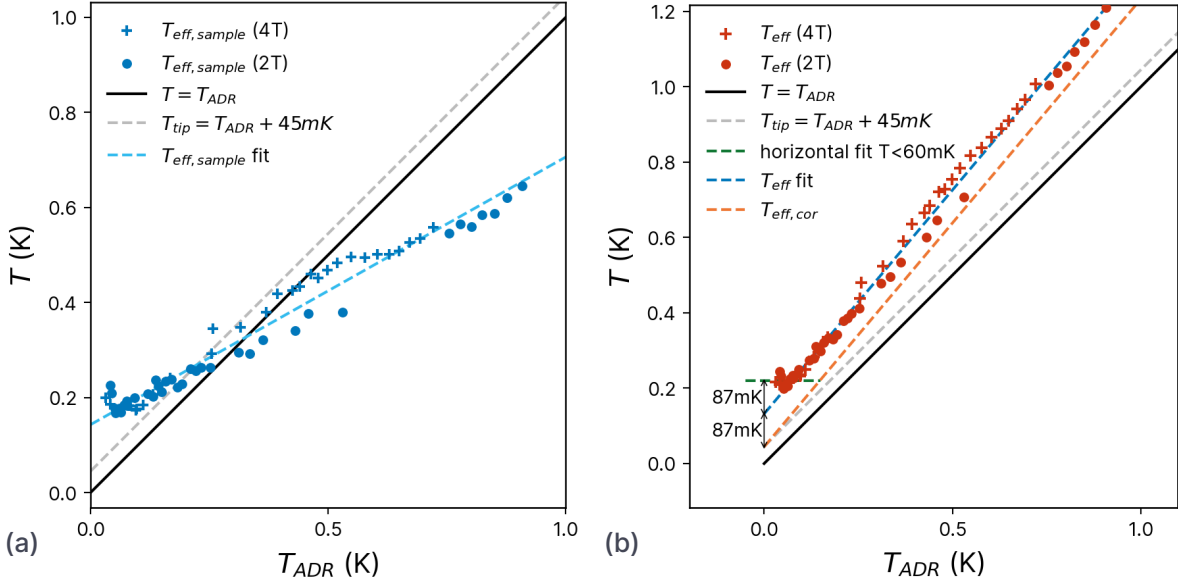


Figure 4.11: Temperature fits of the temperature broadened spin IETS steps for 2 T and 4 T. **(a)** The temperature broadening was deconvoluted twice, as explained in the text. The grey dashed line is the tip temperature $T_{tip} = T_{ADR} + 45\text{ mK}$ and the blue dashed lines is a linear fit. **(b)** The temperature broadening was only deconvoluted once. The green dashed line is a horizontal fit of the minimal temperature plateau and the green dashed line is the linear fit (blue) shifted downwards by 78 mK, for details see text.

ings, the sample temperature T_s can be extracted by fitting the temperature of the second convolution. But as this value also includes other broadening mechanisms, it is more precise to call it an effective temperature $T_{eff,s}$. The extracted $T_{eff,s}$ shown in figure 4.11a indicate a slower temperature increase for the sample than for the tip. Additionally, the fact that of $T_{eff,s}$ increases linearly implies a complex relation $T_{eff,s} \sim T_{ADR}$. As in our STM setup the sample is better thermalized to the position of the temperature sensor than the tip, both the big difference $T_{ADR} - T_{eff,s}$ and the nontrivial dependence seem unrealistic. These considerations are corroborated by noting that T_s will be even lower than $T_{eff,s}$.

In a next step, we fitted spectra like the usual dI/dV curve, i.e. with a rectangular gap function that is smeared by the modulation amplitude and only one Fermi broadening that is left as a fit parameter, which is shown in figure 4.11b. The fitted temperature, denoted by T_{eff} , provides a much more realistic picture: The temperature develops almost parallel in relation to T_{ADR} . For $T < 60\text{ mK}$ the temperature seems to be constant, which count point to a constant instrumental broadening (plus a non-infinite spin lifetime at 0 K). The size of the broadening effects at 0 K can be estimated by subtracting the extrapolated T_{eff} at 0 K from the plateau temperature for $T < 60\text{ mK}$ (dashed green line in figure 4.11b). Removing this broadening effect (87 mK) from the linear fit of T_{eff} (dashed blue line), one obtains the corrected physical broadening $T_{eff,cor}$ (dashed orange line). For $T = 0\text{ K}$ this clearly coincides with T_{tip} , supporting the previous estimate that the temperature of the tip is well described by $T_{tip} = T_{ADR} + 45\text{ mK}$ (dashed gray line).

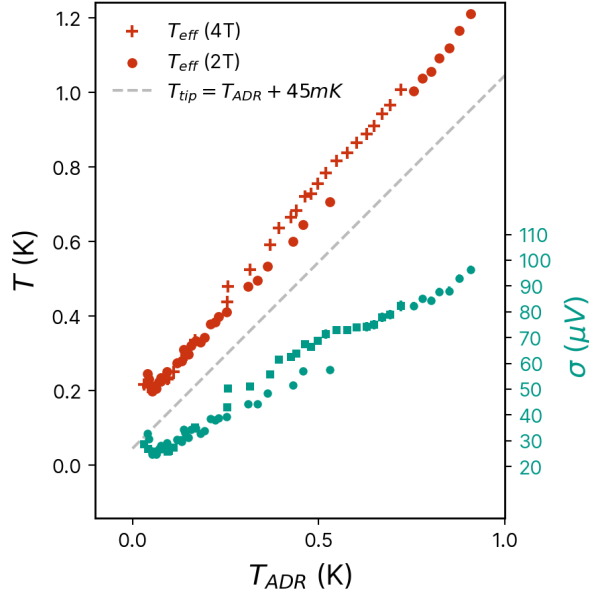


Figure 4.12: Extracting the non-temperature broadening mechanisms: The IETS steps are fitted with a rectangular gap function that is broadened by the modulation amplitude and the fixed tip temperature $T = T_{ADR} + 45\text{ mK}$ (dashed gray line). Additionally, the function is convoluted with a Gaussian, the width σ being a fit parameter (green axis).

The steeper slope of $T_{eff,cor}$ compared to T_{tip} can be attributed to the increased broadening due to a decreasing spin lifetime with growing temperature.

To obtain an estimate for the total broadening contributions apart from temperature and modulation, the gap function is broadened with the modulation amplitude and the fixed tip temperature T_{tip} . Additionally, it is convoluted with a Gaussian, the width σ being a fit parameter. As displayed in figure 4.12, the broadening increases by a factor of four over a temperature range of around 900 mK. By using $\tau = \hbar/(2 * \text{FWHM}) = \hbar/(4 * \sqrt{2 \log 2}\sigma)$ [78] one obtains an upper bound for the lifetime at 0 K of $\tau = 35.4\text{ ps}$

It remains an open question why the single convolution yields more realistic results, compared to the double convolution, which should be used theoretically. We also analyzed spectra of the molecule hanging on the tip at a constant temperature of 1.5 K. The fitted temperatures coincided with the results above, which verifies that during an ADR cycle one can assume thermal equilibrium.

The slight but noticeable difference between the 4 T and the 2 T dataset, see figure 4.12, could be attributed to a different spin lifetime at the two magnetic fields [78]. Other studies have shown no significant temperature dependence of the spin lifetime [79] for magnetic atoms. A more detailed analysis including pump-probe measurements with a spin-polarized tip would be an interesting next step to resolve this issue.

It should be noted that a difference in the temperature of tip and sample would not only have an effect on the resolution of spin IETS spectra: The temperature gradient can also induce a thermovoltage [80] that depends on the logarithmic

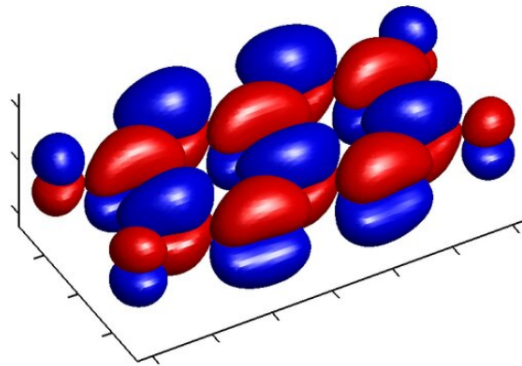


Figure 4.13: Sketch of the LUMO of PTCDA. The lobes of the π -orbital are either below or above the plane of the molecule. The colors mark different signs of the wave function (taken from [82]).

derivative of the sample density of states at the Fermi level. This effect has already been used experimentally [81] where a voltage shift of $10 \mu\text{V}$ per 1K temperature difference was observed, implying that the effect would be very small in our case.

4.8 Conclusion and Comparison to PTCDA

NTCDA and PTCDA are very similar molecules, they only differ in the number of aromatic rings. The smaller the steps in parameter space, the clearer the interpretation of physical differences. This makes the comparison of these two systems so intriguing.

And indeed the molecules share general properties: The Zeemann splitting in high magnetic fields clearly shows that both standing molecules host a spin-1/2 electron system. Also, the bond to the silver adatoms is expected to be similar, as the π -orbital have a very similar shape around the carboxylic oxygen [15, 56], which bond to the dimer. This is supported by the fact that both systems exhibit a Kondo resonance, implying that the coupling to the substrate indeed is of a similar nature. The π -orbital, for PTCDA shown in figure 4.13 and similar for NTCDA, does not have lobes in the molecular plane but only above and below. This suggests little wave function overlap when a bond in that plane is established to an s-shell atom like silver, where the wave function is maximal in the center. This reasoning implies a weak hybridization of the molecules to the substrate and therefore a low Kondo temperature.

The same qualitative behavior of the Kondo effect is also observed when comparing the perturbative line shape fits as shown in figure 4.14a. The model breaks down for both molecules in the experimental temperature range, as the g-factor and the absolute value of $J\rho$ rise significantly for decreasing temperature. The crossover temperature and also the absolute parameters differ noticeably.

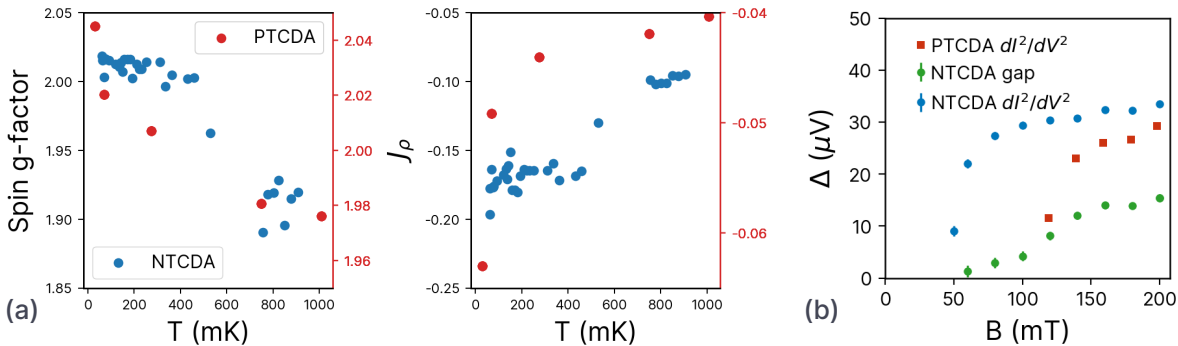


Figure 4.14: Comparison of standing PTCDA and standing NTCDA. **(a)** The fits of the perturbed system for PTCDA with 7 T (red) and NTCDA with 2 T (blue). **(a)** Comparison of the width Δ of the split Kondo peak for NTCDA (red) and NTCDA with two different methods (blue, green).

This is not surprising as the external magnetic field for PTCDA was 7 T and for NTCDA 2 T. A larger perturbing field is expected to minimize the crossover temperature and also the exchange interaction included in J_P [48].

The further comparison does not reveal systematic trends. The $T_K = 109 \pm 16$ mK for NTCDA obtained from the critical field is around three times lower than the $T_K = 291 \pm 13$ mK for PTCDA. The according gap widths of the Kondo peak in low magnetic field are compared in figure 4.14b, which comprises the values from figure 4.4 and figure 2.8a. The widths for PTCDA were acquired with the dI^2/dV^2 method and show the same kink for rising magnetic fields, only that the curve is shifted to higher fields by around 60 mK. The fact that the NTCDA series has more data points below the kink and that additionally an alternative fitting procedure was used, imply a higher precision of the extracted T_K .

On the other hand, the widths of the Kondo peaks give an inverted picture: The single Kondo peak spectrum that was fitted for PTCDA is slimmer than the extracted width at 0 K obtained from the temperature series. The resulting Kondo temperatures are $T_K = 1.28$ K for PTCDA, and $T_K = 1.78 \pm 0.02$ K for NTCDA, respectively.

Due to the discussion above, we take the critical field method as the more reliable one. As mentioned before, the critical field has been used widely in the literature to qualitatively compare T_K . Therefore, it is safe to assume that T_K for the standing NTCDA is lower than for the standing PTCDA. For the physical interpretation, it is sensible to consult the definition of T_K in the Anderson model, which uses parameters of the impurity orbital [41]:

$$k_B T_K = \omega \gamma_0 \sqrt{\frac{U}{4\gamma_0}} \exp\left(-\frac{\pi|\epsilon||\epsilon + U|}{\gamma_0 U}\right), \quad (4.5)$$

where $\omega = 0.4128$ is Wilson's number, ϵ the position of the impurity orbital relative to the Fermi energy, γ_0 the hybridization strength and U the Coulomb repulsion of the degenerate states. As both standing molecules are expected to bond

identically to the substrate, γ_0 can be assumed to be the same. Further, both structures were shown to host a single free spin which translates to $\epsilon < 0$ and $\epsilon + U > 0$. As the LUMO orbital of PTCDA is more extended specially, the Coulomb repulsion U in the orbital will be reduced in comparison to NTCDA. A decreasing U in equation (4.5) results in a higher T_K , which is exactly what we observe. It is noted that an increasing γ_0 would also lead to a higher T_K . From the conducted experiments it is no possible to determine a trend for γ_0 .

4.9 Outlook

To verify if the trend of larger T_K for larger molecules continues, the logical next step would be the repetition of the measurements for the molecule TTCDA, which is larger than PTCDA by three aromatic rings. Another way to tune the system would be to use different atoms as a fundament. It has recently been shown that iron adatoms on Ag(111) can be used to construct a standing PTCDA molecule. Although the magnetic nature of iron is likely to prevent a Kondo effect, this motivates exploration with alternative nonmagnetic substrates, such as copper or gold, given their possession of a single valence electron like silver.

As mentioned before, a possible future experiment is the spin lifetime measurements using pump-probe technique. If the measurements are performed on both molecules, a comparison could verify if the spin lifetime correlates with the Kondo temperature, as expected.

Bibliography

- ¹W. Gerlach and O. Stern, "Der experimentelle Nachweis der Richtungsquantelung im Magnetfeld", *Zeitschrift für Physik* **9**, 349–352 (1922).
- ²W. Pauli, "Zur Quantenmechanik des magnetischen Elektrons", *Zeitschrift für Physik* **43**, 601–623 (1927).
- ³P. A. M. Dirac and R. H. Fowler, "The quantum theory of the electron", *Proceedings of the Royal Society of London. Series A, Containing Papers of a Mathematical and Physical Character* **117**, 610–624 (1997).
- ⁴X. Fan, T. G. Myers, B. A. D. Sukra, and G. Gabrielse, "Measurement of the Electron Magnetic Moment", *Physical Review Letters* **130**, 071801 (2023).
- ⁵G. Binnig, H. Rohrer, Ch. Gerber, and E. Weibel, "Surface Studies by Scanning Tunneling Microscopy", *Physical Review Letters* **49**, 57–61 (1982).
- ⁶G. Binnig, H. Rohrer, Ch. Gerber, and E. Weibel, "7 Reconstruction on Si(111) Resolved in Real Space", *Physical Review Letters* **50**, 120–123 (1983).
- ⁷M. F. Crommie, C. P. Lutz, and D. M. Eigler, "Confinement of Electrons to Quantum Corrals on a Metal Surface", *Science* **262**, 218–220 (1993).
- ⁸R Temirov, S Soubatch, O Neucheva, A. C. Lassise, and F. S. Tautz, "A novel method achieving ultra-high geometrical resolution in scanning tunnelling microscopy", *New Journal of Physics* **10**, 053012 (2008).
- ⁹L. Gross, F. Mohn, N. Moll, P. Liljeroth, and G. Meyer, "The Chemical Structure of a Molecule Resolved by Atomic Force Microscopy", *Science* **325**, 1110–1114 (2009).
- ¹⁰S. Loth, S. Baumann, C. P. Lutz, D. M. Eigler, and A. J. Heinrich, "Bistability in Atomic-Scale Antiferromagnets", *Science* **335**, 196–199 (2012).
- ¹¹S. Baumann, W. Paul, T. Choi, C. P. Lutz, A. Ardavan, and A. J. Heinrich, "Electron paramagnetic resonance of individual atoms on a surface", *Science* **350**, 417–420 (2015).
- ¹²K. Yang, W. Paul, S.-H. Phark, P. Willke, Y. Bae, T. Choi, T. Esat, A. Ardavan, A. J. Heinrich, and C. P. Lutz, "Coherent spin manipulation of individual atoms on a surface", *Science* **366**, 509–512 (2019).

- ¹³R. Temirov, S. Soubatch, A. Lassise, and F. S. Tautz, "Bonding and vibrational dynamics of a large π -conjugated molecule on a metal surface", *Journal of Physics: Condensed Matter* **20**, 224010 (2008).
- ¹⁴R. Temirov, S. Soubatch, A. Luican, and F. S. Tautz, "Free-electron-like dispersion in an organic monolayer film on a metal substrate", *Nature* **444**, 350–353 (2006).
- ¹⁵M. Rohlfing, R. Temirov, and F. S. Tautz, "Adsorption structure and scanning tunneling data of a prototype organic-inorganic interface: PTCDA on Ag(111)", *Physical Review B* **76**, 115421 (2007).
- ¹⁶R. Temirov, A. Lassise, F. B. Anders, and F. S. Tautz, "Kondo effect by controlled cleavage of a single-molecule contact", *Nanotechnology* **19**, 065401 (2008).
- ¹⁷C. Toher, R. Temirov, A. Greuling, F. Pump, M. Kaczmarski, G. Cuniberti, M. Rohlfing, and F. S. Tautz, "Electrical transport through a mechanically gated molecular wire", *Physical Review B* **83**, 155402 (2011).
- ¹⁸C. Wagner, M. F. B. Green, P. Leinen, T. Deilmann, P. Krüger, M. Rohlfing, R. Temirov, and F. S. Tautz, "Scanning Quantum Dot Microscopy", *Physical Review Letters* **115**, 026101 (2015).
- ¹⁹T. Esat, N. Friedrich, F. S. Tautz, and R. Temirov, "A standing molecule as a single-electron field emitter", *Nature* **558**, 573–576 (2018).
- ²⁰T. Esat, M. Ternes, R. Temirov, and F. S. Tautz, "Electron spin secluded inside a bottom-up assembled standing metal-molecule nanostructure", *Physical Review Research* **5**, 033200 (2023).
- ²¹A. Ardavan, O. Rival, J. J. L. Morton, S. J. Blundell, A. M. Tyryshkin, G. A. Timco, and R. E. P. Winpenny, "Will Spin-Relaxation Times in Molecular Magnets Permit Quantum Information Processing?", *Physical Review Letters* **98**, 057201 (2007).
- ²²A. J. Heinrich, W. D. Oliver, L. M. K. Vandersypen, A. Ardavan, R. Sessoli, D. Loss, A. B. Jayich, J. Fernandez-Rossier, A. Laucht, and A. Morello, "Quantum-coherent nanoscience", *Nature Nanotechnology* **16**, 1318–1329 (2021).
- ²³M. Žonda, O. Stetsovych, R. Korytár, M. Ternes, R. Temirov, A. Raccanelli, F. S. Tautz, P. Jelínek, T. Novotný, and M. Švec, "Resolving Ambiguity of the Kondo Temperature Determination in Mechanically Tunable Single-Molecule Kondo Systems", *The Journal of Physical Chemistry Letters* **12**, 6320–6325 (2021).
- ²⁴E. Meyer, R. Bennewitz, and H. J. Hug, "Introduction to Scanning Probe Microscopy", in *Scanning Probe Microscopy: The Lab on a Tip*, edited by E. Meyer, R. Bennewitz, and H. J. Hug, Graduate Texts in Physics (Springer International Publishing, Cham, 2021), pp. 1–12.
- ²⁵R. Wiesendanger, *Scanning probe microscopy and spectroscopy: methods and applications* (Cambridge University Press, Cambridge [England] ; New York, 1994).
- ²⁶J. Bardeen, "Tunnelling from a Many-Particle Point of View", *Physical Review Letters* **6**, 57–59 (1961).

- ²⁷J. Tersoff and D. R. Hamann, "Theory of the scanning tunneling microscope", *Physical Review B* **31**, 805–813 (1985).
- ²⁸B. Voigtländer, *Scanning Probe Microscopy: Atomic Force Microscopy and Scanning Tunneling Microscopy*, NanoScience and Technology (Springer Berlin Heidelberg, Berlin, Heidelberg, 2015).
- ²⁹C. J. Chen, "Theory of scanning tunneling spectroscopy", *Journal of Vacuum Science & Technology A: Vacuum, Surfaces, and Films* **6**, 319–322 (1988).
- ³⁰M. Pivetta, F. Silly, F. Patthey, J. P. Pelz, and W.-D. Schneider, "Reading the ripples of confined surface-state electrons: Profiles of constant integrated local density of states", *Physical Review B* **67**, 193402 (2003).
- ³¹S. G. Davison and M. Stęślicka, *Basic theory of surface states*, Monographs on the Physics and Chemistry of Materials 46 (Clarendon Press ; Oxford University Press, Oxford : New York, 1992).
- ³²R. Gross and A. Marx, *Festkörperphysik*: (OLDENBOURG WISSENSCHAFTSVERLAG, Aug. 2014).
- ³³B. C. Stipe, M. A. Rezaei, and W. Ho, "Single-Molecule Vibrational Spectroscopy and Microscopy", *Science* **280**, 1732–1735 (1998).
- ³⁴A. J. Heinrich, J. A. Gupta, C. P. Lutz, and D. M. Eigler, "Single-Atom Spin-Flip Spectroscopy", *Science* **306**, 466–469 (2004).
- ³⁵J. Lambe and R. C. Jaklevic, "Molecular Vibration Spectra by Inelastic Electron Tunneling", *Physical Review* **165**, 821–832 (1968).
- ³⁶V. Madhavan, W. Chen, T. Jamneala, M. F. Crommie, and N. S. Wingreen, "Tunneling into a Single Magnetic Atom: Spectroscopic Evidence of the Kondo Resonance", *Science* **280**, 567–569 (1998).
- ³⁷W. J. de Haas, J. de Boer, and G. J. van den Berg, "The electrical resistance of gold, copper and lead at low temperatures", *Physica* **1**, 1115–1124 (1934).
- ³⁸G. J. Van Den Berg, "Chapter IV Anomalies in Dilute Metallic Solutions of Transition Elements", in *Progress in Low Temperature Physics*, Vol. 4, edited by C. J. Gorter (Elsevier, Jan. 1964), pp. 194–264.
- ³⁹G. Fiete and E. Heller, "Colloquium: Theory of quantum corrals and quantum mirages", *Reviews of Modern Physics - REV MOD PHYS* **75**, 933–948 (2003).
- ⁴⁰P. W. Anderson, "Localized Magnetic States in Metals", *Physical Review* **124**, 41–53 (1961).
- ⁴¹A. C. Hewson, *The Kondo Problem to Heavy Fermions*, 1st ed. (Cambridge University Press, Jan. 1993).
- ⁴²H. O. Frota, "Shape of the Kondo resonance", *Physical Review B* **45**, 1096–1099 (1992).
- ⁴³D. Jacob, "Temperature evolution of the Kondo peak beyond Fermi liquid theory", *Physical Review B* **108**, L161109 (2023).

- ⁴⁴E. Turco, M. Aapro, S. C. Ganguli, N. Krane, R. Drost, N. Sobrino, A. Bernhardt, M. Juriček, R. Fasel, P. Ruffieux, P. Liljeroth, and D. Jacob, *Accurate Kondo temperature determination of spin-1/2 magnetic impurities*, Oct. 2023.
- ⁴⁵N. Andrei, “Diagonalization of the Kondo Hamiltonian”, *Physical Review Letters* **45**, 379–382 (1980).
- ⁴⁶R. Bulla, “Numerical renormalization group method for quantum impurity systems”, *Reviews of Modern Physics* **80**, 395–450 (2008).
- ⁴⁷C. van Efferen, J. Fischer, T. A. Costi, A. Rosch, T. Michely, and W. Jolie, “Modulated Kondo screening along magnetic mirror twin boundaries in monolayer MoS₂”, *Nature Physics*, 1–6 (2023).
- ⁴⁸M. Ternes, “Spin excitations and correlations in scanning tunneling spectroscopy”, *New Journal of Physics* **17**, 063016 (2015).
- ⁴⁹H. O. Frota and L. N. Oliveira, “Photoemission spectroscopy for the spin-degenerate Anderson model”, *Physical Review B* **33**, 7871–7874 (1986).
- ⁵⁰M. Gruber, A. Weismann, and R. Berndt, “The Kondo resonance line shape in scanning tunnelling spectroscopy: instrumental aspects”, *Journal of Physics: Condensed Matter* **30**, 424001 (2018).
- ⁵¹U. Fano, “Effects of Configuration Interaction on Intensities and Phase Shifts”, *Physical Review* **124**, 1866–1878 (1961).
- ⁵²K. Nagaoka, T. Jamneala, M. Grobis, and M. F. Crommie, “Temperature Dependence of a Single Kondo Impurity”, *Physical Review Letters* **88**, 077205 (2002).
- ⁵³J. Li, W.-D. Schneider, R. Berndt, and B. Delley, “Kondo Scattering Observed at a Single Magnetic Impurity”, *Physical Review Letters* **80**, 2893–2896 (1998).
- ⁵⁴M. Ternes, A. J. Heinrich, and W.-D. Schneider, “Spectroscopic manifestations of the Kondo effect on single adatoms”, *Journal of Physics: Condensed Matter* **21**, 053001 (2009).
- ⁵⁵P. Wahl, L. Diekhöner, G. Wittich, L. Vitali, M. A. Schneider, and K. Kern, “Kondo Effect of Molecular Complexes at Surfaces: Ligand Control of the Local Spin Coupling”, *Physical Review Letters* **95**, 166601 (2005).
- ⁵⁶R. Tonner, P. Rosenow, and P. Jakob, “Molecular structure and vibrations of NTCDA monolayers on Ag(111) from density-functional theory and infrared absorption spectroscopy”, *Physical Chemistry Chemical Physics* **18**, 6316–6328 (2016).
- ⁵⁷J. Ziroff, S. Hame, M. Kochler, A. Bendounan, A. Schöll, and F. Reinert, “Low-energy scale excitations in the spectral function of organic monolayer systems”, *Physical Review B* **85**, 161404 (2012).

- ⁵⁸F. Eickhoff, E. Kolodzeiski, T. Esat, N. Fournier, C. Wagner, T. Deilmann, R. Temirov, M. Rohlfing, F. S. Tautz, and F. B. Anders, “Inelastic electron tunneling spectroscopy for probing strongly correlated many-body systems by scanning tunneling microscopy”, *Physical Review B* **101**, 125405 (2020).
- ⁵⁹T. Esat, P. Borgens, X. Yang, P. Coenen, V. Cherepanov, A. Raccanelli, F. S. Tautz, and R. Temirov, “A millikelvin scanning tunneling microscope in ultra-high vacuum with adiabatic demagnetization refrigeration”, *Review of Scientific Instruments* **92**, 063701 (2021).
- ⁶⁰G. Ventura and L. Risegari, *The art of cryogenics: low-temperature experimental techniques*, 1st ed (Elsevier, Amsterdam ; Boston, 2008).
- ⁶¹T. Esat, X. Yang, F. Mustafayev, H. Soltner, F. S. Tautz, and R. Temirov, “Determining the temperature of a millikelvin scanning tunnelling microscope junction”, *Communications Physics* **6**, 1–10 (2023).
- ⁶²See <http://www.ets-lindgren.com/products/shielding> for ETS-Lindgren. Tech. rep. () .
- ⁶³V. Cherepanov, P. Coenen, and B. Voigtländer, “A nanopositioner for scanning probe microscopy: The KoalaDrive”, *Review of Scientific Instruments* **83**, 023703 (2012).
- ⁶⁴U. Stahl, D. Gador, A. Soukopp, R. Fink, and E. Umbach, “Coverage-dependent superstructures in chemisorbed NTCDA monolayers: a combined LEED and STM study”, *Surface Science* **414**, 423–434 (1998).
- ⁶⁵R. Fink, D. Gador, U. Stahl, Y. Zou, and E. Umbach, “Substrate-dependent lateral order in naphthalene-tetracarboxylic-dianhydride monolayers”, *Physical Review B* **60**, 2818–2826 (1999).
- ⁶⁶L. Kilian, U. Stahl, I. Kossev, M. Sokolowski, R. Fink, and E. Umbach, “The commensurate-to-incommensurate phase transition of an organic monolayer: A high resolution LEED analysis of the superstructures of NTCDA on Ag(111)”, *Surface Science* **602**, 2427–2434 (2008).
- ⁶⁷N. Fournier, “Force-controlled lifting of molecular wires”, *Physical Review B* **84**, 10.1103/PhysRevB.84.035435 (2011).
- ⁶⁸M. F. B. Green, T. Esat, C. Wagner, P. Leinen, A. Grötsch, F. S. Tautz, and R. Temirov, “Patterning a hydrogen-bonded molecular monolayer with a hand-controlled scanning probe microscope”, *Beilstein Journal of Nanotechnology* **5**, 1926–1932 (2014).
- ⁶⁹P. Leinen, M. F. B. Green, T. Esat, C. Wagner, F. S. Tautz, and R. Temirov, “Virtual reality visual feedback for hand-controlled scanning probe microscopy manipulation of single molecules”, *Beilstein Journal of Nanotechnology* **6**, 2148–2153 (2015).
- ⁷⁰<https://github.com/david-jacob/HurwitzFanoFit/blob/main/Python/hurwitzfit.py>.

- ⁷¹T. A. Costi, "Kondo Effect in a Magnetic Field and the Magnetoresistivity of Kondo Alloys", *Physical Review Letters* **85**, 1504–1507 (2000).
- ⁷²S. M. Cronenwett, T. H. Oosterkamp, and L. P. Kouwenhoven, "A Tunable Kondo Effect in Quantum Dots", *Science* **281**, 540–544 (1998).
- ⁷³D. Goldhaber-Gordon, J. Göres, M. A. Kastner, H. Shtrikman, D. Mahalu, and U. Meirav, "From the Kondo Regime to the Mixed-Vалence Regime in a Single-Electron Transistor", *Physical Review Letters* **81**, 5225–5228 (1998).
- ⁷⁴Y.-h. Zhang, S. Kahle, T. Herden, C. Stroh, M. Mayor, U. Schlickum, M. Ternes, P. Wahl, and K. Kern, "Temperature and magnetic field dependence of a Kondo system in the weak coupling regime", *Nature Communications* **4**, 2110 (2013).
- ⁷⁵E. L. Wolf and D. L. Losee, "G-shifts in the "s-d" exchange theory of zero-bias tunneling anomalies", *Physics Letters A* **29**, 334–335 (1969).
- ⁷⁶T. Esat, T. Deilmann, B. Lechtenberg, C. Wagner, P. Krüger, R. Temirov, F. B. Anders, M. Rohlfing, and F. S. Tautz, "Transferring spin into an extended $\{\pi\}$ orbital of a large molecule", *Physical Review B* **91**, 144415 (2015).
- ⁷⁷D. Goldhaber-Gordon, H. Shtrikman, D. Mahalu, D. Abusch-Magder, U. Meirav, and M. A. Kastner, "Kondo effect in a single-electron transistor", *Nature* **391**, 156–159 (1998).
- ⁷⁸A. A. Khajetoorians, S. Lounis, B. Chilian, A. T. Costa, L. Zhou, D. L. Mills, J. Wiebe, and R. Wiesendanger, "Itinerant Nature of Atom-Magnetization Excitation by Tunneling Electrons", *Physical Review Letters* **106**, 037205 (2011).
- ⁷⁹W. Paul, K. Yang, S. Baumann, N. Romming, T. Choi, C. P. Lutz, and A. J. Heinrich, "Control of the millisecond spin lifetime of an electrically probed atom", *Nature Physics* **13**, 403–407 (2017).
- ⁸⁰J. A. Stovneng and P. Lipavský, "Thermopower in scanning-tunneling-microscope experiments", *Physical Review B* **42**, 9214–9216 (1990).
- ⁸¹A. Schneider, M. Wenderoth, K. Engel, M. Rosentreter, A. Heinrich, and R. Ulbrich, "Local electronic structure at steps on Au(111) investigated by the thermovoltage in scanning tunneling microscopy", *Applied Physics A* **66**, S161–S165 (1998).
- ⁸²M. Graus, "Anwendung und Weiterentwicklung der Orbitaltomographie", PhD thesis (Johannes-Maximilians-Universität Würzburg).

Hiermit versichere ich an Eides statt, dass ich die vorliegende Arbeit selbstständig und ohne die Benutzung anderer als der angegebenen Hilfsmittel angefertigt habe. Alle Stellen, die wörtlich oder sinngemäß aus veröffentlichten und nicht veröffentlichten fremden Schriften entnommen wurden, sind als solche kenntlich gemacht. Die Arbeit ist in gleicher oder ähnlicher Form im Rahmen einer anderen Prüfung noch nicht vorgelegt worden.

Valentin Maissen

Valentin Maissen, 8. Dezember 2023